

arXiv:0909.4800v1 [physics.ins-det] 25 Sep 2009

# Simulations of Doppler Effects in Nuclear Reactions for AGATA Commissioning Experiments

ALI AL-ADILI

Nuclear Structure Group

Division of Nuclear and Particle Physics

Department of Physics and Astronomy, Uppsala University

UPPSALA, SWEDEN

2009



## Abstract

The purpose of this master thesis is to simulate suitable nuclear reactions for a commissioning experiment, to be performed with the AGATA  $\gamma$ -ray tracking spectrometer. The main aim of the work is to find a reaction, which gives large Doppler effects of the emitted  $\gamma$  rays, with as small contribution as possible due to the energy and angular spread of the nuclei emitting the  $\gamma$  rays. Inverse kinematics heavy-ion (HI) fusion reactions of the type (HI, $\gamma$ ), (HI, n) on proton and deuteron targets have been studied. Target effects were investigated using the program TRIM in order to determine the impact on the Doppler effects caused by energy and angular straggling in the target material. The cross sections of a large number of reactions of protons and deuterons on nuclei with mass numbers in the range  $A \approx 20 - 100$  have been evaluated using the TALYS reaction code. The fusion-evaporation reactions,  $d(^{51}\text{V}, n)^{52}\text{Cr}$  and  $d(^{37}\text{Cl}, n)^{38}\text{Ar}$  were simulated in detail using the Monte Carlo code evapOR. The interactions in AGATA of the  $\gamma$  rays emitted in these reactions were simulated using GEANT4. The energy resolution of the  $\gamma$  rays after  $\gamma$ -ray tracking and Doppler correction were determined as a function of the interaction position resolution of the germanium detectors. The conclusion of this work is that of the two reactions  $d(^{51}\text{V}, n)^{52}\text{Cr}$  is more suitable for an AGATA commissioning experiment.

# Contents

<b>1</b>	<b>Introduction</b>	<b>3</b>
1.1	Nuclear spectroscopy . . . . .	3
1.2	Motivation . . . . .	4
<b>2</b>	<b>Theory</b>	<b>6</b>
2.1	Nuclear models . . . . .	6
2.1.1	The shell model . . . . .	6
2.1.2	The collective model . . . . .	7
2.1.2.1	Vibrational excitation of spherical nuclei . . . . .	7
2.1.2.2	Permanently deformed nuclei and rotational excitation . . . . .	7
2.2	Nuclear reactions . . . . .	7
2.2.1	Direct reactions . . . . .	7
2.2.2	Compound nucleus reactions . . . . .	8
2.2.2.1	Compound nucleus formation . . . . .	8
2.2.2.2	Compound nucleus decay . . . . .	10
<b>3</b>	<b>Nuclear spectroscopy methods</b>	<b>12</b>
3.1	Interaction of $\gamma$ rays with matter . . . . .	12
3.1.1	Photoelectric effect . . . . .	12
3.1.2	Compton scattering . . . . .	12
3.1.3	Pair production . . . . .	12
3.1.4	Attenuation coefficients . . . . .	13
3.2	Interaction of ions with matter . . . . .	13
3.3	Doppler Effects . . . . .	13
3.4	Gamma-ray spectroscopy . . . . .	14
3.4.1	HPGe detector and energy resolution . . . . .	15
3.5	AGATA . . . . .	15
<b>4</b>	<b>Requirements</b>	<b>18</b>
<b>5</b>	<b>Simulations</b>	<b>19</b>
5.1	TALYS . . . . .	19
5.2	Target effects . . . . .	19
5.2.1	Sources of target effects . . . . .	19
5.3	Fusion-evaporation simulation . . . . .	20
5.4	Simulation of $\gamma$ -ray detection . . . . .	20
5.5	Gamma-ray tracking . . . . .	21
<b>6</b>	<b>Results and discussions</b>	<b>22</b>
6.1	TALYS . . . . .	22
6.1.1	Selected reactions . . . . .	24
6.1.2	Comparison between evapOR and TALYS . . . . .	25
6.2	Studies of target effects . . . . .	26
6.2.1	Energy straggling . . . . .	26
6.2.2	Angular straggling . . . . .	28

6.2.3	Life-time effects . . . . .	29
6.2.4	Experimental determination of the intrinsic FWHM . . . . .	29
6.3	evapOR . . . . .	30
6.3.1	Energy and angular distributions . . . . .	30
6.4	Simulated $\gamma$ -ray spectra . . . . .	32
6.4.1	Graphical illustration of the GEANT4 simulation . . . . .	32
6.4.2	Gamma-ray spectrum produced by summing . . . . .	33
6.4.3	Gamma-ray spectra produced by tracking and Doppler correction . . . . .	34
6.4.4	Doppler effects induced by emission of $\alpha$ particles . . . . .	37
6.4.5	FWHM as a function of smearing parameter . . . . .	37
6.5	Conclusions and summary . . . . .	39
<b>A</b>	<b>Acknowledgment</b>	<b>40</b>
<b>B</b>	<b>Available ion beams at Laboratori Nazionali di Legnaro (Padova)</b>	<b>41</b>
<b>C</b>	<b>Simulation steps</b>	<b>42</b>

# Chapter 1

## Introduction

Within the field of nuclear physics one attempts to describe how the nucleus as a composition of nucleons can be held together, and how the nucleons interact both individually and collectively inside the nucleus. Nuclear models which describe the nuclear structure, can be tested and further developed by improving nuclear detection methods. The chart of nuclides, see figure 1.1, currently consists of about 3500 known nuclides. The green area of the figure 1.1 shows the nuclides located within the drip-lines. According to theoretical calculations less than half of the nuclides are known. In order to produce and study the nuclear structure of these unknown nuclides, great challenges face the development of precise detection instruments. This master thesis aims to design a commissioning experiment to be performed with the new  $\gamma$ -ray spectrometer, Advanced GAMMA Tracking Array (AGATA) [1]. The experiment will be simulated and based on these calculations a possible reaction for the upcoming experiments in 2009 will be proposed.

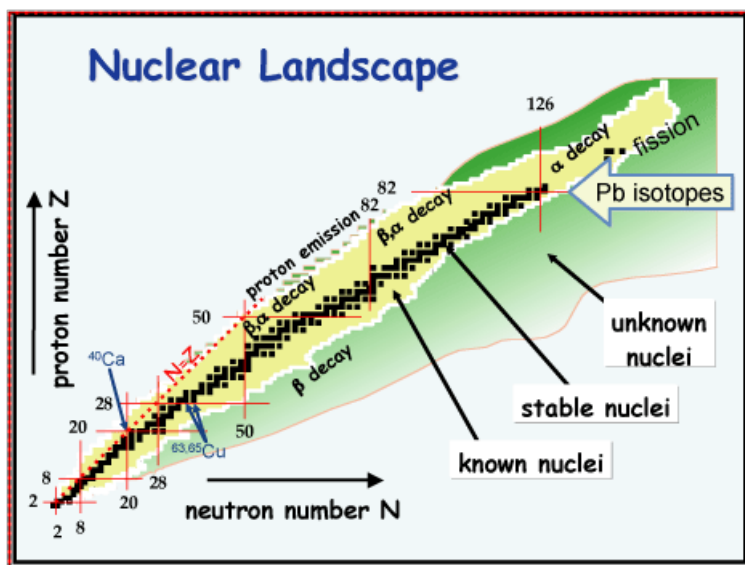


Figure 1.1: Chart of nuclides. (Figure from Holifield Radioactive Ion Beam Facility, Oak Ridge <http://www.phy.ornl.gov>)

### 1.1 Nuclear spectroscopy

Spectroscopy early became an effective way of revealing information about the atomic and sub-atomic quantal systems. In atomic physics, studies of emission spectra corresponding to the transitions between electronic orbits, was a key element in understanding the atom. Nuclear physicists also use spectroscopic tools, by which one may retrieve valuable information about the inner struc-

ture of the nuclei. The energy levels (states) of the nuclei are denoted by their spin ( $J$ ), and parity ( $\pi$ ), as ( $J^\pi$ ). The de-excitation process of the states occurs either through emission of particles ( $e^-$ ,  $\alpha$ , p...) or  $\gamma$  rays. The  $\gamma$  radiation emitted by the de-exciting nucleus spans an energy range from a few keV to tens of MeV. Gamma-ray spectroscopy plays a pivotal role in discovering new exotic nuclei far beyond the line of stability. Theoretical models can be evaluated and improved by testing them with the experimental data obtained by using  $\gamma$ -ray spectroscopic tools. Among the  $\gamma$ -ray spectroscopy instruments used so far, the high-purity germanium detector (HPGe) is the most successful one. By assembling a large number of such detectors in an array surrounding the position of the nuclear reaction, one can obtain efficient and precise detection of the emitted  $\gamma$  rays.

One major factor contributing to the uncertainty in the measured  $\gamma$ -ray spectra is the Doppler effect. Considering in-beam experiments, the nuclei emitting  $\gamma$  radiation are usually not at rest in the laboratory frame; hence the measured energy of the  $\gamma$  rays is subject to an uncertainty caused by the Doppler effect. If not corrected for, this will lead to the broadening of the  $\gamma$ -ray spectra. The Doppler effect depends on two factors, the velocity of the nucleus and the angle between the direction of motion of the nucleus and the emitted  $\gamma$  ray. Due to the second factor, the first interaction point of the  $\gamma$  ray in the detector should be determined in order to minimize the Doppler effects on the broadening of the  $\gamma$ -ray peaks. One main advantage with new  $\gamma$ -ray spectrometers compared with previous instruments, is the  $\gamma$ -ray tracking technique, by which the first interaction point can be determined with much better precision than before, which enhances the Doppler correction capabilities. At present two such  $\gamma$ -ray spectrometers are being developed, AGATA [2] in Europe and GRETA [1] in USA.

## 1.2 Motivation

It is of great interest to study how one can compensate for the Doppler broadening of the  $\gamma$ -ray peaks in order to achieve a higher energy resolution with the AGATA spectrometer. The task of this work was to find a suitable nuclear reaction, in which the Doppler shifted  $\gamma$  rays can be studied using one AGATA triple cluster detector in an experiment to be performed at INFN/LNL in Italy.

One of the aims of this experiment is to use the Doppler effects to determine the interaction position resolution of the AGATA germanium detectors. Figure 1.2 shows a schematic view of the experimental setup. The reaction in study is

$$A + a \rightarrow B + b, \tag{1.1}$$

where  $A$  is the accelerated ion colliding with target  $a$ . The products after the collision are the particle  $b$  and the residual nucleus  $B$ , which emits the Doppler shifted  $\gamma$  ray.

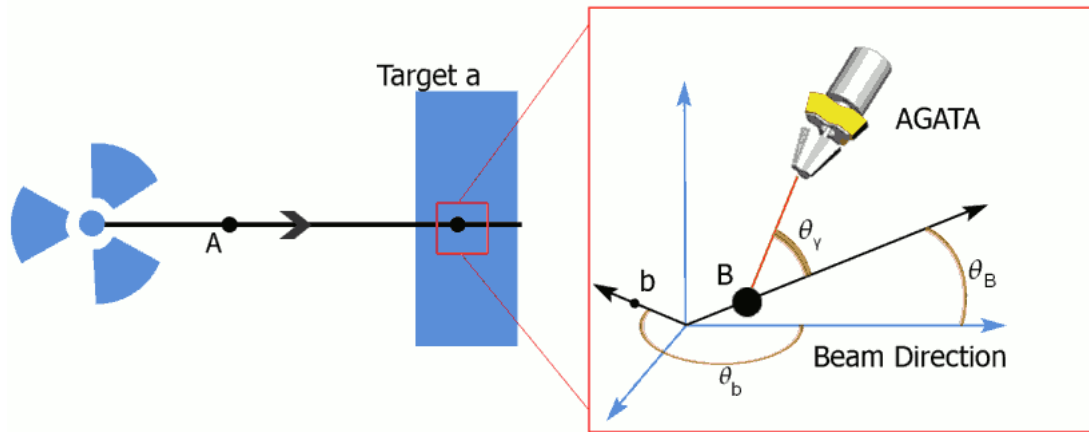


Figure 1.2: A schematic view of the experiment where the ion  $A$  from the accelerator collides with the target  $a$ .  $\theta_B$  and  $\theta_b$  are the angle of emission of the residual nucleus and the emitted particle respectively, and  $\theta_\gamma$  is the angle between of the direction of the residual nucleus  $B$  and the emitted  $\gamma$  ray.

# Chapter 2

## Theory

### 2.1 Nuclear models

There are essentially two classes of nuclear models. The first class is called *independent particle models*, where the Pauli principle restricts the collisions of the nucleons inside the nucleus, leading to a large mean free path. The shell model belongs to this class. The second class of models assumes strongly interacting nucleons inside the nucleus, resulting in a small mean free path. The nuclear liquid drop model belongs to this class. In general these models are called *collective models* as they attempt to describe phenomena that involve the nucleus as a whole, e.g. vibrations and rotations.

In this chapter brief descriptions of the shell model and of the collective model are given.

#### 2.1.1 The shell model

According to the Pauli principle the fermions cannot occupy the same quantum state. Therefore nucleons can orbit almost freely inside the nucleus, similarly to the electrons in the atom. In the atom, electrons are moving in a central potential caused by the positively charged nucleus. In the nucleus, the potential is created by the nucleons themselves through the nucleon-nucleon interaction. In the shell model, the nucleons move in a central potential usually parametrized as

$$V(r) = \frac{V_0}{1 + e^{(r-R)/a}} + V_{\ell s}(r) \vec{\ell} \cdot \vec{s}. \quad (2.1)$$

The first term in equation 2.1 is the *Woods Saxon potential* with the parameters: potential depth  $V_0$ , diffuseness parameter  $a$ , nuclear radius  $R = r_0 A^{2/3}$  ( $A$  is the nucleon number and  $r_0$  is the radius parameter). The second term is the spin-orbit interaction, where the spin ( $\vec{s}$ ) and angular momentum ( $\vec{\ell}$ ) vectors can be oriented either parallel or anti-parallel in the total nucleon spin quantum number  $\vec{j} = \vec{\ell} \pm \frac{1}{2}$ .

The single-particle model is an extreme shell model form where the nucleons move freely in a central potential without interacting with each other. An odd- $A$  nucleus in this model is composed of an inert even-even core, plus an unpaired nucleon. The last unpaired nucleon determines the nuclear properties, such as spin and parity. All known even-even nuclei have spin and parity  $J^\pi = 0^+$  in the ground state. By introducing a residual force in the shell model, called pairing, one can explain the ground state spin and parity of even-even nuclei. The pairing interaction implies an attractive force between pairs of nucleons with opposite orbital angular momenta in identical orbits. The strongest attractive interaction occurs for nucleon pairs with largest possible quantum numbers  $m_j$  of opposite sign, i.e.  $m_j = +j$  and  $m_j = -j$ . The quantum number  $m_j$  is the projection of  $j$  on a quantization axis and can have values from  $-j$  to  $j$ . The spin and parity of each pair of nucleons in identical orbits with  $\pm m_j$  is  $0^+$ . The attractive pairing interaction leads to an increase of the binding energy for a completely paired nucleus with total spin and parity  $0^+$ , compared with one with any number of non-paired nucleons.

The shell model can explain the presence of magic proton ( $Z$ ) and neutron ( $N$ ) numbers in the nuclei. By including the spin-orbit term in the potential, the shell model gives the magic numbers



$Z, N = 2, 8, 20, 28, 50, 82, 126$ , which corresponds to strongly bound nuclei at filled shells. Experimental results verify these theoretical shell model predictions. Doubly magic nuclei have magic proton and neutron numbers. The few nuclei which are doubly magic are strongly bound, like e.g.  ${}^4\text{He}$ .

### 2.1.2 The collective model

Two major modes of collective excitations are described within this model, namely vibrational and rotational excitations [3].

#### 2.1.2.1 Vibrational excitation of spherical nuclei

The nucleus experiences oscillations which could either change the size leaving the shape constant (*breathing mode*), or change the shape and leaving the density constant. The latter is more usual and can be explained by different modes of oscillations. The surface of a nucleus oscillating around a spherical equilibrium shape is written as

$$R(\theta, \phi, t) = R_0 \left( 1 + \sum_{\lambda=0}^{\infty} \sum_{\mu=-\lambda}^{\lambda} \alpha_{\lambda\mu}(t) Y_{\lambda\mu}(\theta, \phi) \right), \quad (2.2)$$

where  $\alpha_{\lambda\mu}(t)$  is the time dependent shape parameter,  $R_0$  is the radius of the sphere, and  $Y_{\lambda\mu}(\theta, \phi)$  are the spherical harmonics. The multipolarity  $\lambda$  determines the oscillation type, with  $\lambda = 0$  corresponding to monopole oscillations. These oscillations have no angular dependency. Dipole oscillations occur when  $\lambda = 1$ , causing the nucleus to vibrate around a fixed laboratory reference point. The value of  $\lambda = 2$  implies quadrupole oscillations in which the nucleus alternates between prolate and oblate shape. The energy levels of these vibrational modes are given by

$$E_{N,\lambda} = \hbar\omega_\lambda \sum_{\mu=-\lambda}^{\lambda} (n_{\lambda\mu} + 1/2) = \hbar\omega_\lambda \left( N_\lambda + \frac{1}{2}(2\lambda + 1) \right), \quad (2.3)$$

where  $N_\lambda$  is the number of phonons in the nuclear vibration. A phonon is one quantum of vibrational energy, in analogy with the photon being the electromagnetic quantum. The frequency is given by  $\omega_\lambda$ . An increase of the number of phonons implies higher energies, for a vibrational mode  $\lambda$ . These energies will form a ladder with increasing  $\hbar\omega_\lambda$ . This spectral phenomenon is called a *vibrational band* [4].

#### 2.1.2.2 Permanently deformed nuclei and rotational excitation

The spherical symmetry is broken when moving away from closed shells. Due to the pairing effect mentioned in 2.1.1, the nucleons outside closed shells, will occupy the largest possible  $\pm m_j$  values, which leads to a non-spherical shape. The existence of permanent deformations will open up the possibility for nuclear rotations, which are not present in spherically symmetric nuclei. Due to the rotation the nucleus feels a centrifugal stretching since it is not a rigid body. In analogy with vibrational bands, rotations form *rotational bands*.

## 2.2 Nuclear reactions

Nuclear reactions can be *elastic*, if the target and the projectile are in the same states before and after the reaction (usually in their ground states). When excited states are formed or new particles are created, the collision is *inelastic* [5]. When nuclei collide with each other many reaction types can occur. Direct reactions and compound reactions are two important types of reactions.

### 2.2.1 Direct reactions

In a direct reaction the projectile can undergo stripping in which case some of the nucleons are transferred from the projectile to the target. An example of a stripping reaction is (d,p). A

knockout reaction can also occur, in which the incident nucleus knocks out nucleons from the target nucleus, as in a (p,np) reaction. Direct reactions occur on a very short time scale,  $10^{-22}$  to  $10^{-23}$ s [3], and do not change the structure of the projectile and the target dramatically.

### 2.2.2 Compound nucleus reactions

According to [5], compound nucleus reactions occur when two nuclei form an intermediate state. The compound nucleus formation between nuclei  $a$  and  $A$  is depicted as



where  $X^*$  is the excited compound nucleus and  $R$  is the excited residual nucleus. The timescales of these reactions are relatively long, roughly  $10^{-16}$  to  $10^{-18}$ s. The information about the constituents before the collision is permanently destroyed, hence the output decay channels is independent of the compound nucleus formation. If the same compound nucleus is reached through another reaction, say  $c + C \rightarrow X^*$  with different colliding nuclei, the probability of the decay channel  $X^* \rightarrow R^* + \sum \text{particles}$  remains the same. This hypothesis is called *the independence hypothesis* and it implies that it is possible to separate the cross section  $\sigma$ , into the formation cross section  $\sigma_{aA}^{\text{CN}}$  for projectile  $a$  and target  $A$ , and the branching ratio  $G_{Bb}^{\text{CN}}$  (CN=compound nucleus) for the decay to particle  $b$  and nucleus  $B$ :

$$\sigma = \sigma_{aA}^{\text{CN}}(E)G_{Bb}^{\text{CN}}(E). \quad (2.5)$$

The cross section term  $\sigma_{aA}^{\text{CN}}(E)$  is the probability of the compound nucleus formation at the center of mass energy  $E$ . As the compound nucleus must decay, the sum of all the partial decays is  $\sum_i G_i^{\text{CN}}(E) = 1$ . The excitation energy  $E_{\text{CN}}^*$  of the compound nucleus can be expressed as

$$E_{\text{CN}}^* = \frac{Z_A + N_A}{Z_A + N_A + Z_a + N_a} E_{\text{lab}} + [m_a + m_A - m_{\text{CN}}] c^2, \quad (2.6)$$

where  $E_{\text{lab}}$  is the kinetic energy of the projectile in the laboratory frame and the masses  $m_a$ ,  $m_A$  and  $m_{\text{CN}}$  are the atomic masses of the projectile, target, and compound nucleus, respectively. The compound nucleus de-excites through particle evaporation.

#### 2.2.2.1 Compound nucleus formation

Depending on the collision type and the impact parameter, high orbital angular momenta may be transferred to populate the compound nucleus. The maximum amount of angular momentum transfer in the compound nucleus reaction, is denoted with  $\ell_{\text{cr}}$  [6]. By considering other reaction types, higher  $\ell$  values can be reached. Figure 2.1 shows the differential cross section  $d\sigma/dl$  as a function of  $\ell$ .

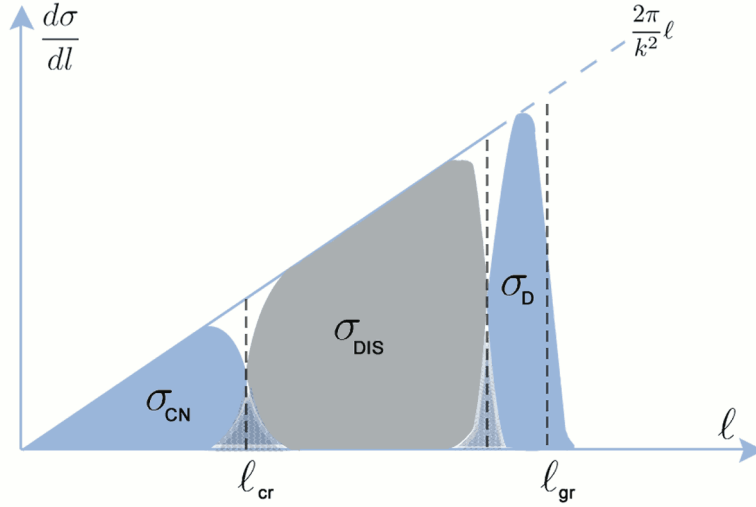


Figure 2.1: Differential cross section as a function of orbital angular momentum.

Direct reactions occur for peripheral collisions implying high angular momentum transfers. When the total angular momentum transfer  $\ell_{gr}$  is reached, the cross section drops. The *sharp cut-off model* states that this drops instantly when  $\ell_{gr}$  is reached. This assumes a well-defined nuclear radius and a behavior similar to the classical rigid-body collision. But since experiments show that the nuclear radius is diffuse, and the border is not well-defined, the collision may not fall drastically when  $\ell_{gr}$  is reached. Instead of this sharp cut-off model, a smooth drop-off model is showed in figure 2.1 [5, 6].

The angular momentum transfer is essential in order to understand the probabilities for nuclear reactions. According to the statistical model, for heavy-ion collisions, the reaction cross section for the compound formation depends on the transfer of orbital angular momentum  $\ell$  as [6]

$$\sigma_{Aa}^{CN}(E) = \pi k^{-2} \sum_0^{\infty} (2\ell + 1) T_{\ell} P_{\ell}^{CN}, \quad (2.7)$$

where  $T_{\ell}$  is the transmission coefficient,  $k$  is the wave number, and  $P_{\ell}^{CN}$  is the probability of the  $\ell$ -wave to enter the compound nucleus. In compound reactions the transmission coefficient  $T_{\ell}$  approximately equals unity for relatively high angular momenta. The cross section can be simplified into

$$\sigma_{Aa}^{CN}(E) = \pi k^{-2} \sum_0^{\ell_{cr}} (2\ell + 1) P_{\ell}^{CN}. \quad (2.8)$$

The sum runs from orbital angular momentum 0 until the critical value  $\ell_{cr}$  in which value the compound nucleus formation cross section rapidly drops to zero.

The cross section for final formation and decay is finally given by [7]

$$\sigma_{Aa \rightarrow i} = \sum_{J_c} \sigma_{Aa}^{CN}(E) \frac{\Gamma_i(E_i, J_c)}{\sum_j \Gamma_j(E_j, J_c)} = \sum_{J_c} \left( \pi k^{-2} \sum_{S=|I-s|}^{I+s} \sum_{\ell=|J_c-S|}^{J_c+S} \frac{(2J_c+1)}{(2s+1)(2I+1)} T_{\ell}(E) \right) \frac{\Gamma_i}{\sum_j \Gamma_j}, \quad (2.9)$$

where  $\sigma_{aA}(E)$  is the compound nucleus formation cross section, dependent on the entrance channel-energy  $E$ . The decay width  $\Gamma_i$  is for a specific final state  $i$  in the exit channel. The target spin is given by  $I$ , and  $S$  is the channel spin. The projectile spin is represented by  $s$ .

### 2.2.2.2 Compound nucleus decay

When the compound nucleus is formed it populates energy levels high above the ground state. The nucleus then tries to reach the ground state through an evaporation process in which mainly light particles (neutrons, protons,  $\alpha$  particles) are subsequently emitted in a so called cascade, see figure 2.2. While charged particles, such as protons and  $\alpha$  particles, have to overcome the Coulomb barrier in order to escape the excited nucleus, neutral particles do not. This will be reflected in the energy distribution of the emitted particles: neutrons are emitted with lower kinetic energies. See figures 6.14 and 6.21 for a comparison of energy distributions of neutrons and alpha particles.

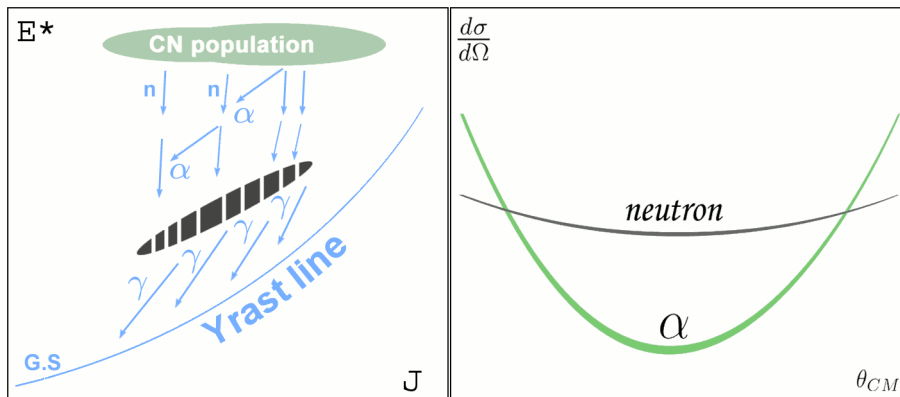


Figure 2.2: In the left figure a population scheme is shown, in which compound nuclei are created with a given excitation energy  $E^*$ . Particle evaporation releases most of the energies, followed by  $\gamma$  ray cascades to finally reach the ground state. In the right figure the angular distribution of neutrons and  $\alpha$  particles are schematically presented, indicating an increased anisotropy for the  $\alpha$  particles.

Alpha particles carry away larger values of angular momentum from the compound nucleus than neutrons and protons, as shown in figure 2.2. This follows since

$$\vec{\ell} = \vec{r} \times \vec{p} = \vec{r} \times m \vec{v} \quad (2.10)$$

and both the mass  $m$ , and the velocity  $v$ , is higher for  $\alpha$  particles than for neutrons and protons.

#### Energy distribution of evaporated particles

The energy distributions of the evaporated particles have a Maxwell-Boltzmann shape, according to the spin dependent statistical model. Following the derivation of Lang and Lecouteur [8], the probability of emission is

$$W_p(E^*, J, E_R^*, J_R) = \frac{2S_p + 1}{\pi^2 \hbar^3} \mu E_p \sigma_{\text{inv}}^J(E^*) \frac{\rho(E_R^*, J_R)}{\rho(E^*, J)}, \quad (2.11)$$

where the emitted particle has a reduced mass  $\mu$ , energy  $E_p$ , and spin  $S_p$ . The inverse compound nucleus production cross section is  $\sigma_{\text{inv}}^J(E^*)$ , and  $\rho(E^*, J)$  and  $\rho(E_R^*, J_R)$  are the level densities of the initial and residual nuclei at spin and excitation energy  $E^*$ ,  $J$  and  $E_R^*$ ,  $J_R$ , respectively.

#### Angular distribution of evaporated particles

Based on the work of Ericson and Strutinsky [9], the orbital angular momentum of the incident particle is orthogonal to the direction of the beam. The total angular momentum aligns preferably in the plane perpendicular to the beam axis. The angular distribution is symmetric with respect to the angle  $90^\circ$  relative to the direction of the incoming beam. According to [6, 9], the angular distribution of the evaporated particles can be written as

$$W_{J,\ell}(\theta_p, E_p) = \frac{1}{4\pi} \sum_k^{\infty} (-1)^k (4k+1) \left( \frac{(2k)!}{(2^k k!)} \right)^2 j_{2k} \left( \frac{iJ\ell}{\sigma_f^2} \right) P_{2k}(\cos \theta_p). \quad (2.12)$$

The spherical Bessel functions  $j_{2k}$  are of order  $2k$  and  $\theta_p$  is the angle between the incident beam and the direction of the emitted particle in the center of mass system. The spin cut-off parameter of the residual nucleus is given by  $\sigma_f$ . The Legendre polynomial  $P_{2k}$  is even, thus there is a symmetry around  $90^\circ$ . Figure 2.2 illustrates that  $\alpha$  particles are emitted mostly at large ( $\sim 180^\circ$ ) and small ( $\sim 0^\circ$ ) angles. The reason for this is that they remove large values of the angular momentum  $\ell$  when evaporated from the compound nucleus. For neutrons the evaporation is nearly isotropic. See figure 6.12 for an angular distribution of neutrons obtained by the simulations performed in this work.

# Chapter 3

## Nuclear spectroscopy methods

### 3.1 Interaction of $\gamma$ rays with matter

When  $\gamma$  rays enter matter, three interaction types can occur, photoelectric effect, Compton scattering and pair production.

#### 3.1.1 Photoelectric effect

When irradiating a metal surface with light above a certain frequency, an electric current will flow. Einstein found that electrons are removed from the metal and that the photon is absorbed by the atom [10]. The photo-electron can only be ejected when the photon energy is higher than the binding energy of the electron. The kinetic energy for the photoelectron is given by

$$E_e^{\text{kin}} = E_\gamma - B_e, \quad (3.1)$$

where  $E_\gamma$  is the photon energy and  $B_e$  is the electronic binding energy. The photoelectric effect dominates at low  $E_\gamma$  (see figure 3.1).

#### 3.1.2 Compton scattering

When the photon energy increases, the probability of photon scattering with electrons increases (see figure 3.1). According to Compton in his article from 1923 [11], the observed photon wavelength  $\lambda$  increases after the interaction, leading to a decreasing energy, since  $E = hc/\lambda$ . Recoil energy is transferred from the photon to the electron. Due to energy and momentum conservation, one arrives at the Compton scattering formula which gives the energy of the scattered  $\gamma$  ray

$$E'_\gamma = \frac{E_\gamma}{1 + (E_\gamma/mc^2)(1 - \cos \theta_C)}. \quad (3.2)$$

Here  $E_\gamma$  is the initial energy of the  $\gamma$  ray, and  $m$  is the mass of the electron. the scattering angle of the photon is  $\theta_C$ .

#### 3.1.3 Pair production

If the photon energy is large enough, pair production may occur, i.e. creation of an electron-positron pair, as  $\gamma \rightarrow e^+ + e^-$ . The minimum energy required is 1.022 MeV. Due to momentum and energy conservation this process is only possible if it occurs nearby a particle with non-zero rest mass, e.g. a nucleus [12].

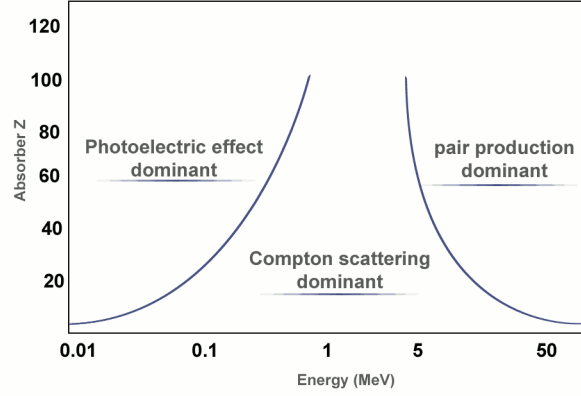


Figure 3.1: Domains of electromagnetic interaction with matter. [12]

### 3.1.4 Attenuation coefficients

The intensity of a beam passing through matter, decreases exponentially

$$I = I_0 e^{-\mu \delta}, \quad (3.3)$$

where  $I_0$  is the incident beam intensity,  $\mu$  is the total attenuation coefficient and  $\delta$  is the material thickness. The probability for a photon removal per unit length is given by  $\mu$ . The total attenuation coefficient is the sum of the attenuation coefficients for the photoelectric effect ( $\tau$ ), Compton scattering ( $c$ ) and pair production ( $\kappa$ )

$$\mu = \tau + c + \kappa. \quad (3.4)$$

The inverse of the attenuation coefficient is equal to the mean free path of the  $\gamma$  rays

$$\lambda_m = \frac{1}{\mu}. \quad (3.5)$$

## 3.2 Interaction of ions with matter

Transport of ions in matter is mainly affected by electromagnetic interactions with the electrons of the material. Rutherford scattering, i.e. scattering between nuclei, is rare in comparison with the interaction with the electrons. The energy loss of the ion per distance traveled is given by [13]

$$-\frac{dE}{dx} = \left( \frac{e^2}{4\pi\epsilon_0} \right)^2 \frac{4\pi z^2 N_0 Z \rho}{mv^2 A} \left[ \ln \left( \frac{2mv^2}{I(1 - (v/c)^2)} \right) - \frac{v^2}{c^2} \right], \quad (3.6)$$

where  $A$ ,  $Z$ ,  $z$ ,  $E$  and  $v$  are the mass number, atomic number, electric charge, energy and velocity of the ion respectively,  $m$  is the electron mass,  $\rho$  the density of the target,  $I$  is the mean excitation potential of the target, and  $N_0$  Avogadro's number.

## 3.3 Doppler Effects

Doppler Effects are an important concept for nuclear spectroscopy. Gamma radiation emitted by a nucleus in motion, appears to have a different energy than the actual transition energy. The frequency of the  $\gamma$  rays is lower if the nucleus moves away from the observer, and higher when it

moves towards the observer. Figure 3.2 demonstrates the change of frequency  $f$ , which is observed by the receiver as  $f'$ .

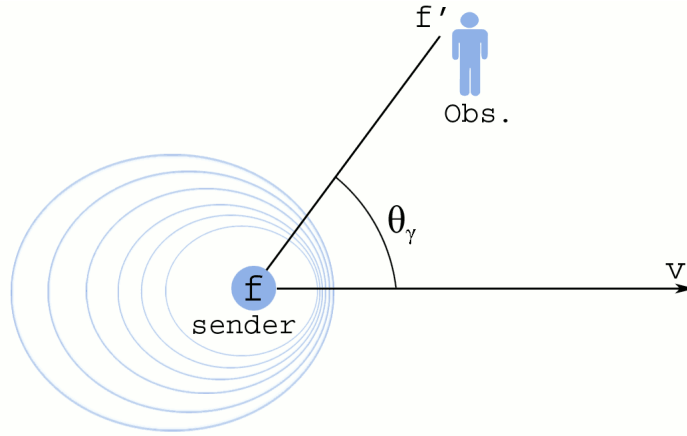


Figure 3.2: Illustration of the Doppler shift.

The relativistic version of the Doppler shift formula for a source moving with velocity  $v$  is [14]

$$E_\gamma = E_{\gamma_0} \frac{\sqrt{1 - \frac{v^2}{c^2}}}{1 - \frac{v}{c} \cos \theta_\gamma}, \quad (3.7)$$

where  $E_\gamma$  and  $E_{\gamma_0}$  ( $E = hf$ ) are the measured  $\gamma$ -ray energy and the  $\gamma$ -ray transition energy, respectively, and  $\theta$  is the angle between the receiver and the direction of motion of the source. The velocities in the simulations of the AGATA commissioning experiments are below 10 % of the speed of light, hence the relativistic factor  $\sqrt{1 - v^2/c^2}$  is very close to unity. In this case a simplified non-relativistic approximation of equation 3.8 is appropriate to use:

$$E_\gamma = E_{\gamma_0} \left( 1 + \frac{v}{c} \cos \theta_\gamma \right). \quad (3.8)$$

### 3.4 Gamma-ray spectroscopy

When photons enter a  $\gamma$ -ray detector they may deposit all or part of their energy in the detector. Figure 3.3 shows how different interactions contribute to a typical  $\gamma$ -ray spectrum.

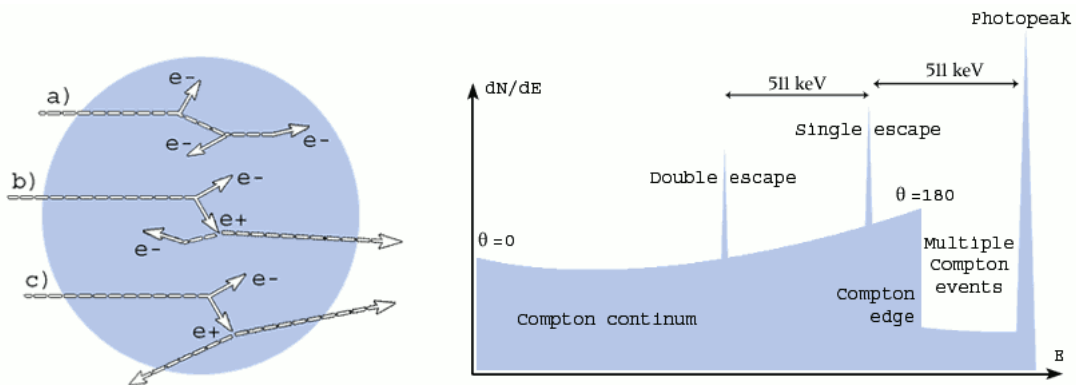


Figure 3.3: Three  $\gamma$ -rays enter the detector in the left figure. a) Two Compton scatterings followed by a photoelectric effect. b) A pair production followed by single escape. c) Pair production followed by double escape. The figure on the right shows the main characteristics of a  $\gamma$ -ray spectrum.



Photons depositing all their energy in the detector give rise to the full-energy peak (photopeak) while the ones that do not deposit all their energy, but escape after one or more Compton scatterings, contribute to the Compton continuum. The scattering angle in equation 3.2, determines the energy deposited. Back-scattering of the photons forms the Compton edge in figure 3.3. The amount of  $\gamma$  rays that escape from the detector depends on the size of the detector compared to the mean free path of the photons in the detector.

### 3.4.1 HPGe detector and energy resolution

The high-purity germanium (HPGe) detector is undoubtedly the most successful instrument for spectroscopic studies of the nuclear structure. The superior performance of the HPGe detector is mainly due to its excellent energy resolution, which allows the distinction of  $\gamma$  rays with close lying energies. The energy resolution is characterized by the full width at half maximum (FWHM) of the  $\gamma$ -ray peaks. Two factors contribute to the FWHM, here labeled  $W$  [15]:

$$W = \sqrt{W_i^2 + W_D^2}. \quad (3.9)$$

The intrinsic width  $W_i$  is caused by the properties of the detector itself and consists of three terms: the electronic noise  $W_{\text{en}}$ , which is independent of the measured  $\gamma$ -ray energy, the statistical factor  $W_{\text{sf}}$ , which depends on the square root of the energy, and the incomplete charge collection  $W_{\text{cc}}$ , which is proportional to the energy,

$$W_i = \sqrt{W_{\text{en}}^2 + W_{\text{sf}}^2 + W_{\text{cc}}^2}. \quad (3.10)$$

The second factor  $W_D$  is due to the Doppler effects and it is non-zero only if the  $\gamma$  ray is emitted by a moving source. The Doppler factor consists of three terms:

$$W_D = \sqrt{W_{\theta_\gamma}^2 + W_{\theta_r}^2 + W_{v_r}^2}. \quad (3.11)$$

$W_{\theta_\gamma}$  is due to the broadening caused by the uncertainty in the determination of the emission angle of the  $\gamma$  ray,  $\theta_\gamma$ . This term depends on the position resolution of the first interaction point in the detector. The terms  $W_{\theta_r}$  and  $W_{v_r}$  are due to the uncertainty in the determination of the angle and velocity, respectively, of the residual nucleus.

## 3.5 AGATA

AGATA is a  $\gamma$ -ray spectrometer which in its final  $4\pi$  configuration will consist of 180 HPGe crystals assembled in 60 triple cluster detectors (see figure 3.4). Each HPGe crystal is of type closed-end coaxial. The crystals are 9 cm long, have circular shape with a diameter of 8 cm at the rear end, and a hexagonal shape in the front. The crystals are also electrically segmented into 6 longitudinal and 6 azimuthal segments which together with the core gives 37 separate signals per crystal. The crystals are encapsulated in aluminum cans (see figure 3.4).



Figure 3.4: The AGATA HPGe detectors [2].

AGATA will use advanced digital electronics and pulse-shape analysis (PSA) techniques to determine the 3D position and the energy deposition in each  $\gamma$ -ray interaction point. An example of the PSA technique is shown in figure 3.5. The interaction points determined by the PSA are then fed into a  $\gamma$ -ray tracking algorithm, which is based on the Compton scattering formula, equation 3.2, and by which the full-energy and the first interaction point of each  $\gamma$  ray is reconstructed.

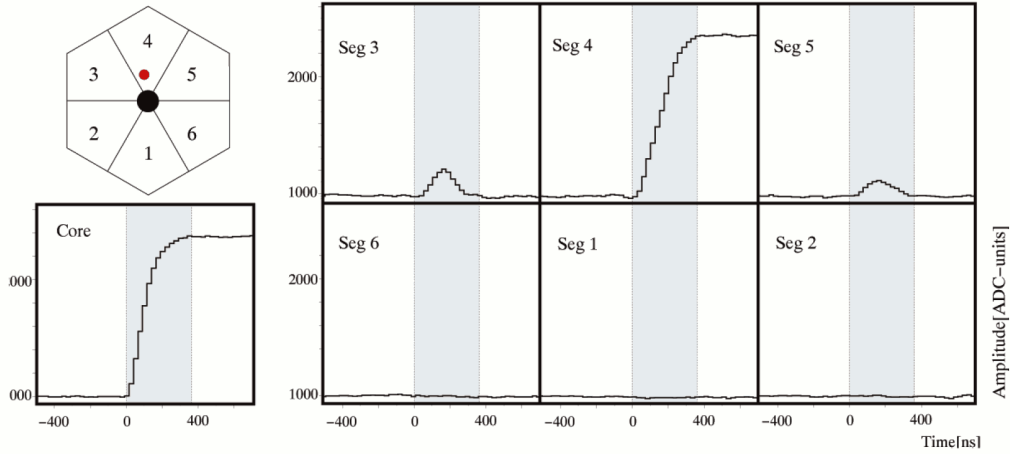


Figure 3.5: Illustration of the pulse shape technique. In this event a hit in segment 4 can be seen. A signal is registered from the core and two mirror charges are seen in segments 3 and 5 [16].

The improvement to be expected by AGATA compared to earlier Ge-detector arrays, not based on  $\gamma$ -ray tracking, will result in a larger full-energy efficiency and much better Doppler correction capabilities. With previous detector arrays one could only determine which detector was hit by a  $\gamma$  ray. Thus, one had an opening angle corresponding to the diameter of the detector, typically  $\sim 5$  cm. In AGATA the position resolution will be about 5 mm which will lead to a much smaller value of  $W_{\theta_\gamma}$  in equation 3.11 and, thus, too much narrower  $\gamma$ -ray peaks.

AGATA will serve as a powerful tool to understand nuclear structure far from the  $\beta$ -stability line. Several detection difficulties such as Doppler broadening will be possible to compensate for using the AGATA spectrometer. By having a better resolution of the full-energy peaks, weak transitions in exotic nuclei can be studied [2]. Figure 3.6 displays the predicted performance of the AGATA demonstrator compared to the CLARA spectrometer.

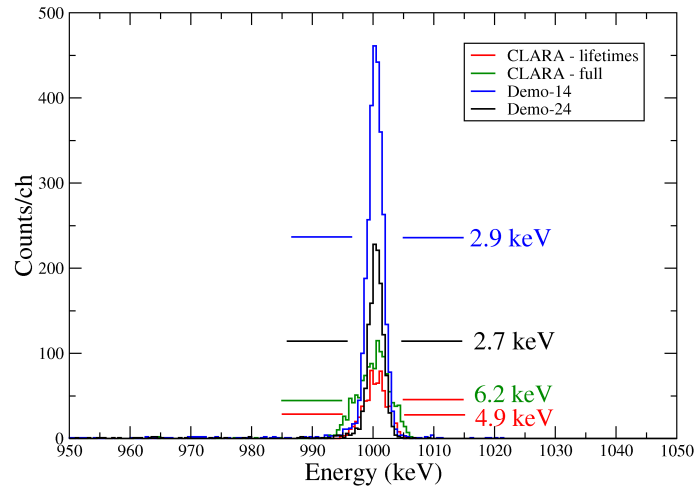


Figure 3.6: The predicted performance of the AGATA demonstrator (15 HPGe crystals) compared to the CLARA spectrometer, which consists of about 100 non-segmented HPGe crystals. The FWHM at a  $\gamma$ -ray energy of 1 MeV is more than a factor of two better with AGATA (2.7 keV and 2.9 keV) at a target to detector front face distance of 24 and 14 cm, respectively, than with the full CLARA array (6.2 keV) [17].

# Chapter 4

## Requirements

The selection of reactions to be studied in this work was based on the following list of criteria.

- Large Doppler shifts: This is required in order to study the interaction position resolution of the AGATA detectors. The velocity of the residual nucleus should be higher than 5 % of the speed of light.
- Large reaction rate: The reaction rate is given by

$$R = \frac{I}{q} \frac{\rho t \sigma}{m_A N_A}, \quad (4.1)$$

where  $I$  is the ion beam current,  $q$  the electric charge of the ions,  $t$  and  $\rho$  the target thickness and density, respectively,  $\sigma$  the cross section,  $m_A$  the atomic weight, and  $N_A$  Avogadro's number.

- Available ion beams at LNL: The available beams at the LNL accelerator laboratory are listed in appendix B.
- Competing decay channels: Different particle evaporation channels compete. Proton and  $\alpha$  particle evaporation give large recoil energies to the residual nucleus, since they need high kinetic energy to penetrate the Coulomb barrier. Neutrons do not face the same situation, hence the average recoil energy given to the nucleus is smaller.
- Position of  $\gamma$ -ray emission: In order not to have  $\gamma$ -ray emission inside the target, the life times must be longer than the time it takes for the ions to pass the target material. To have a negligible influence on the Doppler effects, the life times must be short enough so that the decay occurs within 1 mm after the target.
- Energy and angular straggling of the ions in the target should be as small as possible.
- Gamma-ray energies: A minimum  $\gamma$ -ray energy of 500 keV is required. Lower energies will give smaller Doppler shifts, which are harder to study.
- Strong  $\gamma$ -ray transitions: In even-even nuclei a strong  $2^+ \rightarrow 0^+$  transition is often observed, therefore even-even final nuclei are preferred.

In this work two reaction types were studied in order to find a suitable reaction: a) proton capture  $p(X, \gamma)$  or deuteron capture  $d(X, \gamma)$  and b) fusion evaporation with emission of one neutron followed by  $\gamma$  rays, for example  $p(X, n\gamma)$  or  $d(X, n\gamma)$ . Both type of reactions were of inverse kinematics type, with a heavy ion beam on a proton or deuteron target.

# Chapter 5

## Simulations

### 5.1 TALYS

The code used to evaluate the cross sections was TALYS, a comprehensive nuclear reaction modeling code [18]. The projectiles and ejectiles in TALYS can be of type  $\gamma$  rays, neutrons,  $^1\text{-}^3\text{H}$ ,  $^3\text{-}^4\text{He}$ , with energies in the range 0.1 to 200 MeV. The mass number of the target can be in the range  $A=12$  to  $A=339$ . Note that by TALYS it is not possible to simulate the reactions in inverse kinematics. TALYS was, however, used for calculating the cross sections of the reactions, which are independent of the reaction being of normal or inverse kinematics type. In this work the results obtained with TALYS were in several cases compared to experimental data taken from the National Nuclear Data Center.

The total probability of a reaction to happen, i.e. the total cross section  $\sigma_{\text{tot}}$ , is the sum of the elastic  $\sigma_e$  and the inelastic cross section  $\sigma_{\text{ie}}$ :

$$\sigma_{\text{tot}} = \sigma_e + \sigma_{\text{ie}}. \quad (5.1)$$

The inelastic cross section is a sum of the compound nucleus, pre-equilibrium and direct cross sections. The compound nucleus formation cross section  $\sigma_{\text{cf}}$ , is defined as the difference between the reaction  $\sigma_{\text{reac}}$  and the direct cross section  $\sigma_{\text{direct}}$ :

$$\sigma_{\text{cf}} = \sigma_{\text{reac}} - \sigma_{\text{direct}}. \quad (5.2)$$

The output of TALYS contains the calculated cross sections for non-elastic direct reactions, non-elastic and elastic compound nucleus reactions, and non-elastic pre-equilibrium reactions.

### 5.2 Target effects

The target that will be used in the experiment has an effect on the velocity and direction of the ions. The program used for studies of the target effects was TRIM [19], which is a Monte Carlo based program that simulates collisions between incident ions and atoms in the target material. Angular and energy distributions of the incident ions are obtained from the TRIM simulations. The target material can be chosen from a list of chemical substances and compounds.

#### 5.2.1 Sources of target effects

When the ions enter the target material they are deflected due to the electromagnetic interaction primarily with the electrons. Thus, the ions will lose energy and deviate from the beam direction, which leads to so called energy and angular straggling of the ions. There are two main aspects of the target effects in the simulations.

1. **Position of the reaction in the target.** If the reaction occurs in the beginning of the target, the residual nucleus will experience energy and angular straggling, whereas if the reaction occurs at the end, the incident ion instead of the residual nucleus will lose kinetic

energy. The difference both in kinetic energy and atomic number of the incident ion and residual nucleus leads to the difference in straggling.

2. **Neutron energy and angular distribution.** After the reaction the excited compound nucleus is formed, and particles are emitted. Depending on the energy and angular distribution of the particles, the residual nucleus will obtain different kinetic energies. The recoil due to the neutron evaporation will either boost the nucleus or slow it down. Since this happens inside the target material the energy and angular straggling will change after the reaction. Two extreme cases were investigated, one where the neutron is emitted at about  $0^\circ$  relative to the ion beam, and the other where it is emitted in at about  $180^\circ$ .

### 5.3 Fusion-evaporation simulation

The fusion-evaporation simulations were done using the Monte Carlo code `evapOR` [20]. This program allows for fusion of two arbitrary nuclei, followed by evaporation of particles which can be of 7 different types (n, p, d, a, t,  $^3\text{He}$ ,  $^6\text{Li}$ ) as well as emission of  $\gamma$  rays. It uses the statistical model for compound nucleus reactions, described in section 2.2.2.

In `evapOR` the velocity of the emitted particle in the laboratory system,  $\vec{v}_{p,\text{LAB}}$ , is obtained by adding the velocity of the compound nucleus in the laboratory system  $\vec{v}_{\text{CN,LAB}}$  and the velocity of the particle in the center of mass system  $\vec{v}_{p,\text{CM}}$ :

$$\vec{v}_{p,\text{LAB}} = \vec{v}_{\text{CN,LAB}} + \vec{v}_{p,\text{CM}}. \quad (5.3)$$

The transformation of the particle emission angle between the center of mass  $m$  and laboratory systems is given by

$$\tan \theta_{p,\text{LAB}} = \frac{\sin \theta_{p,\text{CM}}}{\cos \theta_{p,\text{CM}} + x}, \quad (5.4)$$

where

$$x = \left[ \frac{m_a m_b}{m_A m_B} \frac{E}{E + Q} \right]^{1/2}. \quad (5.5)$$

Here  $Q$  denotes the Q-value of the decay,  $m_a$ ,  $m_A$ ,  $m_b$ ,  $m_B$  are the masses of initial and final products, and  $E$  the center of mass energy of the impinging particle.

An output file with the format shown in table 5.1 is produced by `evapOR`.

	Index	Energy	vx	vy	vz
<b>Start new event</b>	\$				
<b>Compound nucleus (Z,N)</b>	101 (18,39)	63090	0	0	1
<b>Emitted particle (<math>\alpha</math>)</b>	7	3615.4	-0.81693864	-0.13911782	0.55969405
$\gamma$	1	2169.5	0	1	0

Table 5.1: Example of the .aga output file produced by `evapOR`. In the output shown here, the  $\gamma$  ray is emitted in the y direction. The parameters vx, vy, vz are the normalized ( $|\vec{v}|=1$ ) velocities in Cartesian coordinates in the laboratory system. The indices 101, 7 and 1 denote the compound nucleus, an alpha particle and a  $\gamma$  ray respectively. Energy is the kinetic energy of the particle in the laboratory system or the Doppler shifted  $\gamma$ -ray energy, all given in keV.

The event shown in table 5.1 starts with the compound nucleus. The listed  $\gamma$  ray was not generated by `evapOR` but was added artificially [21]. The energy of the  $\gamma$  ray is Doppler shifted according to the non-relativistic Doppler formula of eq. (3.7).

### 5.4 Simulation of $\gamma$ -ray detection

The complex geometry of the AGATA detectors have been implemented in the GEANT4 simulation package [22, 23]. In this package, one can choose between using a single HPGe crystal or any number of triple clusters up to the full  $4\pi$  AGATA array.

One can either generate particles in GEANT4 or get them from an external event file. In the present simulations event files from evapOR was used as input to GEANT4. The output of an ordinary run using an input event file similar to the output shown in table 5.1, is shown in table 5.2.

	Index	Energy   v/c	x	y	z
<b>Start new event</b>	-100				
<b>Compound nucleus velocity</b>	-101	v/c=0.05889	0N	0N	1N
<b>Position of CN</b>	-102		0	0	0
<b>Emitted particle (<math>\alpha</math>)</b>	-7	3303.4	-0.04844N	-0.89261N	-0.44821N
<b>Residual nucleus</b>	-101	v/c=0.06147	0.00175 N	0.03233 N	0.99948 N
<b>Position of RN</b>	-102		0	0	0
<b>Emitted particle <math>\gamma</math></b>	-1	2172.300	0N	1N	0N
<b>Interaction point 1 (detector 2)</b>	2	383.495	-0.373	43.248	-0.426
<b>Interaction point 2 (detector 2)</b>	2	32.573	-1.477	43.844	-1.851
<b>Interaction point 3 (detector 2)</b>	2	34.293	-7.208	49.511	-2.958
<b>RN after emitted <math>\gamma</math></b>	-101	v/c=0.06147	0.00175 N	0.03133 N	0.99951 N
<b>Position of RN</b>	-102		0	0	0
<b>RN after emitted <math>\gamma</math></b>	-8	66971.702	0.00175 N	0.03133 N	0.99951 N

Table 5.2: Example of an output file of the AGATA GEANT4 package. N denotes that the velocity of the residual nucleus is normalized to 1. Energies are given in keV and positions in cm. RN stands for the residual nucleus.

The events start (Index=-100) with the compound nucleus velocity divided by the speed of light in vacuum,  $c$ , and its direction (-101), followed by the position of the CN (-102), the evaporated particle (-7), and the residual nucleus (-101, -102). The nucleus then emits the Doppler shifted  $\gamma$ -ray (-1), which interacts three times in detector number 2 (Index=2). After this the  $v/c$  and the direction (-101) and position (-102) of the residual nucleus is listed. Finally the kinetic energy and the direction of the residual nucleus is given (-8).

## 5.5 Gamma-ray tracking

The next step is to track the  $\gamma$  rays [16]. In this work the MGT tracking program [24] was used. This tracking code uses the Compton scattering formula to determine the path of the  $\gamma$  ray in the detectors and gives the full energy and the first interaction point of the incoming  $\gamma$  ray. The first interaction point provides the angle  $\theta_\gamma$  needed for the Doppler correction according to equation 3.7.

In the planned AGATA commissioning experiment, no ancillary detectors for the detection of the residual nuclei will be used, therefore the velocity vectors of the residual nucleus will be unknown experimentally. Instead all the residual nuclei are assumed to have the average velocity and direction along the beam axis.

# Chapter 6

## Results and discussions

### 6.1 TALYS

In table 6.1 the studied reactions are summarized. Following the requirements in chapter 4, most of the ion beams at LNL [appendix B] were excluded from further study. In most reactions, competition between different reaction channels were found. The  $\gamma$ -ray energy was also in many cases lower than required. The proton and deuteron capture reactions had too small cross sections to be useful for the planned AGATA commissioning experiment, hence only fusion evaporation reactions were studied.

p - Reactions	Result	d - Reactions	Result
$^{19}\text{F} + \text{p}$	$\alpha$ channel dominates	$^{27}\text{Al} + \text{d}$	Competing p & n channels
$^{63}\text{Cu} + \text{p}$	p channel dominates	$^{63}\text{Cu} + \text{d}$	Competing n, p & $\alpha$ channels
$^{81}\text{Br} + \text{p}$	n ch. dominates, odd-even nucleus	$^{107}\text{Ag} + \text{d}$	Channels competing
$^{27}\text{Al} + \text{p}$	$\alpha$ & p channels competing	$^{28}\text{Si} + \text{d}$	p channel dominates
$^{31}\text{P} + \text{p}$	p channel dominates	$^{37}\text{Cl} + \text{d}$	<b>n channel dominates</b>
$^{35}\text{Cl} + \text{p}$	p channel dominates	$^{51}\text{V} + \text{d}$	<b>n channel dominates</b>
$^{58}\text{Ni} + \text{p}$	p channel dominates	$^{100}\text{Mo} + \text{d}$	p channel dominates
$^{56}\text{Fe} + \text{p}$	p channel dominates	$^{94}\text{Mo} + \text{d}$	p channel dominates
$^{28}\text{Si} + \text{p}$	p channel dominates	$^{81}\text{Br} + \text{d}$	p & n channels competing
$^{32}\text{S} + \text{p}$	p channel dominates		
$^{33}\text{S} + \text{p}$	p channel dominates		
$^{65}\text{Cu} + \text{p}$	n ch. dominates, bad $\gamma$ energy		

Table 6.1: Proton and deuteron reactions studied by TALYS.



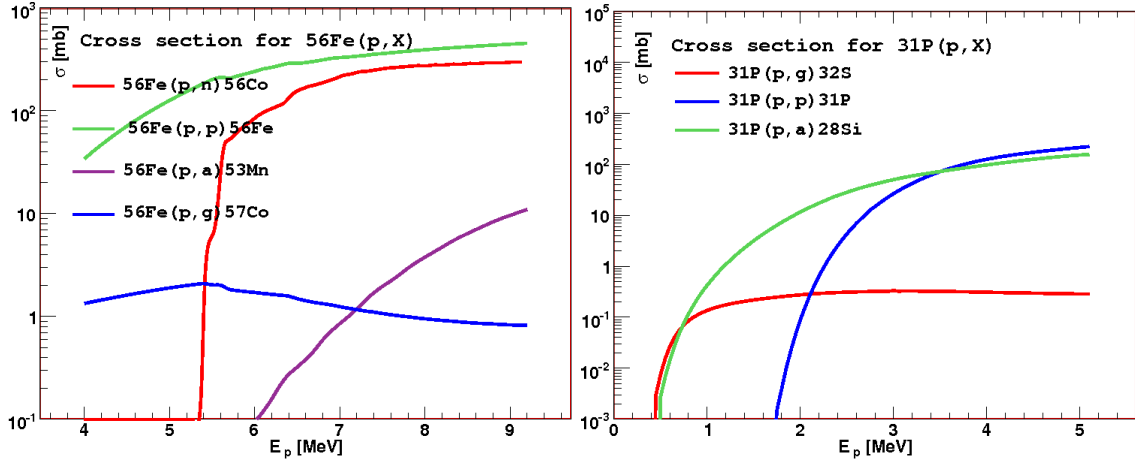


Figure 6.1: Example of two (p,n) reactions,  $^{56}\text{Fe}(p, X)$  and  $^{31}\text{P}(p, X)$ . (a= $\alpha$  particle, g= $\gamma$  ray). The energy of the incident proton is given in the laboratory system.

In the left plot of figure 6.1 the  $^{56}\text{Fe}(p, p)^{56}\text{Fe}$  reaction channel is dominant. In the right plot of figure 6.1, the  $\alpha$  emission dominates up to  $\sim 3$  MeV at which energy proton emission starts to become important.

Two examples of deuteron induced reactions are presented in figure 6.2. To the left,  $^{28}\text{Si}(d, X)$ , where the proton channel dominates. In figure 6.2,  $^{27}\text{Al}(d, X)$  is shown, where there is a competition between the neutron and proton channels.

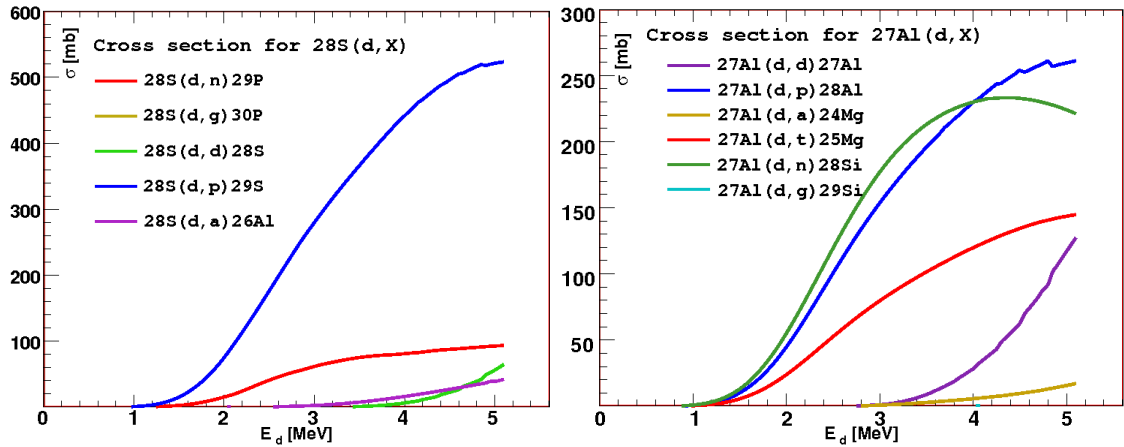


Figure 6.2: Example of two (d,n) reactions,  $^{28}\text{Si}(d, X)$  and  $^{27}\text{Al}(d, X)$ . The energy of the incident deuteron is given in the laboratory system.

Results obtained from the TALYS simulations were verified against experimental data. Three examples of such comparisons are presented in figures 6.3 and 6.4.

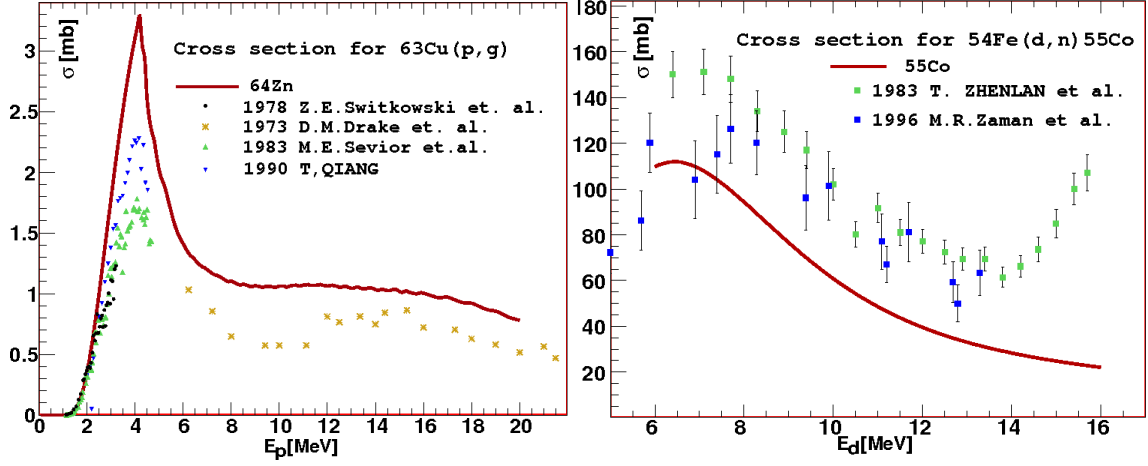


Figure 6.3: In the left figure the reaction  $^{63}\text{Cu}(d, n)$  is compared to measurements reported in ref. [25, 26, 27, 28]. In the right figure  $^{54}\text{Fe}(d, n)$  is compared to experimental results from ref. [29, 30]. The incident proton and deuteron energies are given in the laboratory system.

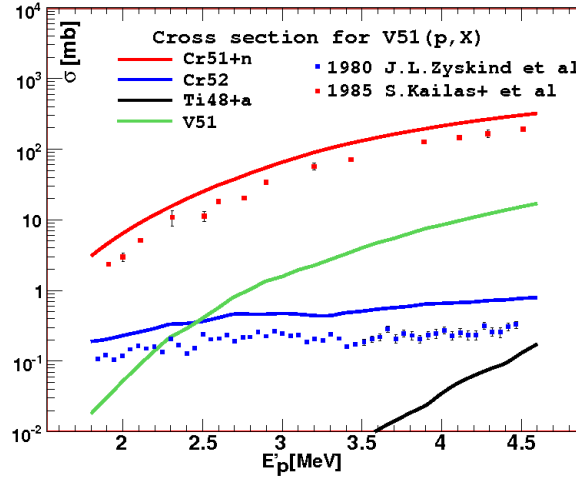


Figure 6.4: The  $^{51}\text{V}(p, n)$  reaction compared to experimental results from ref. [31, 32]. The energy of the incident proton is given in the laboratory system.

For the  $^{63}\text{Cu}(p, \gamma)$  reaction (figure 6.3 left), four independent measurements were plotted together with the calculation of TALYS. The differences are small at low energies but reach a factor of 2 around the peak at  $E_p \approx 4$  MeV. In the plot on the right hand side of figure 6.3, the experimental values are close to the results of the TALYS calculation for the  $^{54}\text{Fe}(d, n)$  reaction for energies up to about 14 MeV. At higher energies the measurements of ref. [29] differ from the TALYS calculations. In figure 6.4 the reaction  $^{51}\text{V}(p, X)$  is simulated and compared with measurements from ref. [31, 32]. Both the neutron and  $\gamma$ -ray emission channels are close to the results obtained from measurements.

### 6.1.1 Selected reactions

In table 6.1 two reactions were shown with a dominating neutron emission channel. These are the reactions that were further studied. Both reactions leads to an even-even residual nucleus, and they have appropriate life times. The first reaction,  $^{37}\text{Cl}(d, n)^{38}\text{Ar}$ , leads to  $^{38}\text{Ar}$  which has a first excited state  $2^+$  at 2168 keV. The high  $\gamma$ -ray energy which decays to the  $0^+$  ground state is very good for the Doppler-effect measurements. The cross-section calculation from TALYS is shown in the upper plot of figure 6.5. The reaction  $^{37}\text{Cl}(d, n)^{38}\text{Ar}$  is clearly dominating.

The second reaction,  $^{51}\text{V}(d, n)^{52}\text{Cr}$ , is for the same reason a suitable reaction. The first excited state has an excitation energy of 1434 keV. The calculated cross section for this reaction is shown in the lower plot of figure 6.5.

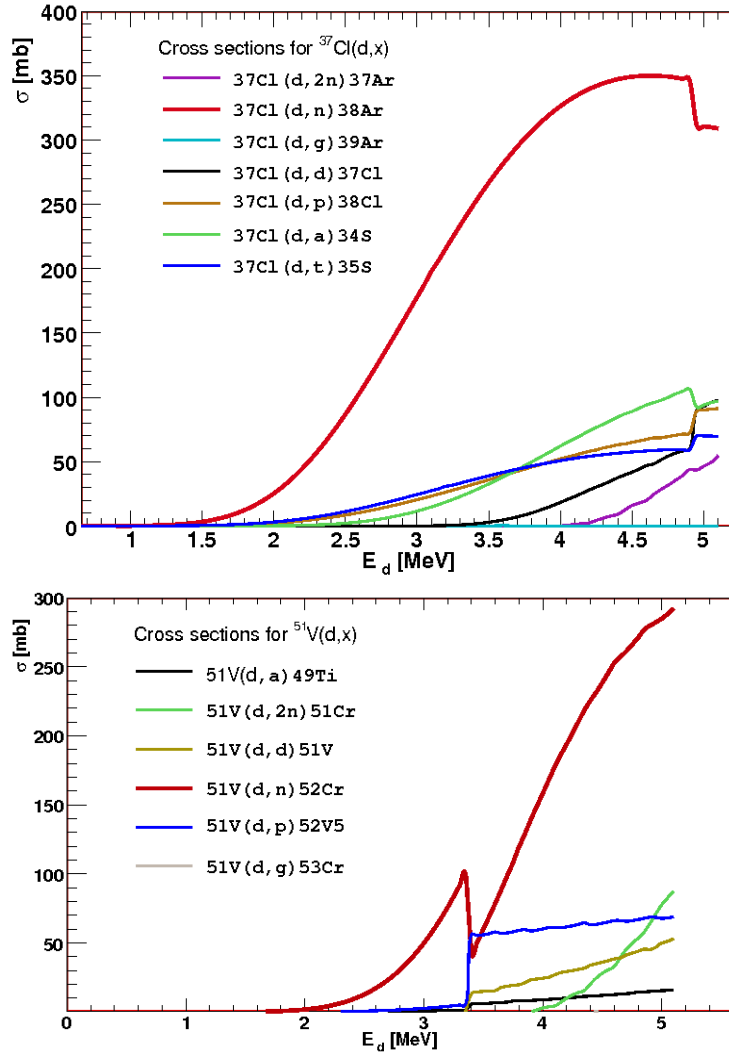


Figure 6.5: TALYS cross-section calculations for  $^{37}\text{Cl}(d, n)\text{Ar}$  and  $^{51}\text{V}(d, n)\text{Cr}$ . The incident deuteron energies are given in the laboratory system.

The cross section of the reaction  $^{37}\text{Cl}(d, n)^{38}\text{Ar}$  reaches a maximum of about 350 mb at a deuteron energy of about 4 MeV. The cross section of the  $^{51}\text{V}(d, n)^{52}\text{Cr}$  reaction has a local maximum at about  $E_{d, \text{LAB}} = 3.4$  MeV and it increases at higher energies without competition with other channels. Based on the TALYS results, both reactions,  $d + ^{37}\text{Cl}$  and  $d + ^{51}\text{V}$ , are suitable for further studies. The energies chosen are  $E_d = 3.8\text{MeV}$  and  $E_d = 3.2\text{MeV}$  for the  $d + ^{37}\text{Cl}$  and  $d + ^{51}\text{V}$  reactions respectively. In inverse kinematics reactions thus correspond to  $E_{^{37}\text{Cl}} = 70.0$  MeV and  $E_{^{51}\text{V}} = 81.6$  MeV, respectively.

### 6.1.2 Comparison between evapOR and TALYS

To verify the calculations, a comparison between TALYS and evapOR was made. The results for the  $d + ^{51}\text{V}$  reaction are presented in figure 6.6.

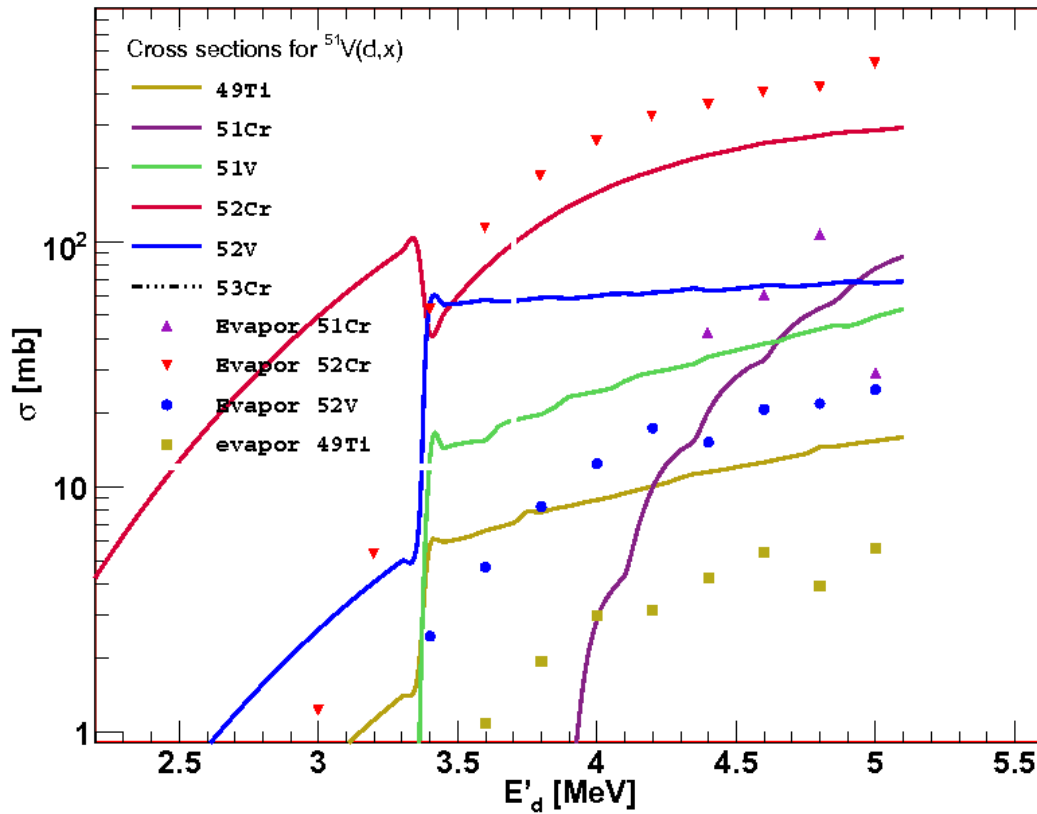


Figure 6.6: Comparison of cross sections obtained by TALYS (lines), and evapOR (symbols) for the  $d + {}^{51}\text{V}$  reaction. The incident deuteron energy is given in the laboratory system.

As seen in figure 6.6, large discrepancies were obtained. Below  $E \approx 3.4$  MeV the TALYS and evapOR results are closer. Above 3.4 MeV the cross sections are similar in particular for the  ${}^{51}\text{V}(d, n){}^{52}\text{Cr}$  reaction.

## 6.2 Studies of target effects

In the proposed commissioning experiment, an inverse kinematics reaction will be used. This means that for the two selected reactions,  $d + {}^{37}\text{Cl}$  and  $d + {}^{51}\text{V}$ , deuterium would be the target nucleus. One possible target is to use a thin plastic foil (e.g. polyethylene) enriched in deuterium. Such foils do, however, only allow very weak beam currents without the foil getting destroyed (melting). Instead it is proposed to use a deuterated Ti foil which can contain about 1 deuterium atom per titanium atom[33]. The chosen target thickness is  $200 \mu\text{m}/\text{cm}^2$ . No deuterated titanium compound is available in TRIM therefore pure titanium was chosen as target in the simulation. The difference in energy straggling due to this is expected to be negligible. No nuclear reactions will occur between the  ${}^{37}\text{Cl}$  or  ${}^{51}\text{V}$  beams and the Ti nuclei of the target (the energies are well below the Coloumb barrier).

### 6.2.1 Energy straggling

The target studies were based on the two effects presented in section 5.2.1, due to the neutron distribution and the position of the reaction. Here only results of the study of the reaction  $d + {}^{51}\text{V}$  are presented. The results of the target studies for the  $d + {}^{37}\text{Cl}$  reaction are very similar. In order to study the effect of different neutron emission angles, two events with relatively high and low residual nucleus ( ${}^{52}\text{Cr}$ ) kinetic energies were chosen from the evapOR simulation. The energies were  $E_{RN1} = 82.4$  MeV and  $E_{RN2} = 73.6$  MeV in the laboratory system. The difference is due

to the neutron emission angle: the event with energy  $E_{RN1}$  had a large neutron emission angle,  $\theta_{n,CM} = 174.4^\circ$  while the event with  $E_{RN2}$  had a small angle,  $\theta_{n,CM} = 6.7^\circ$ . The energies  $E_{RN1}$  and  $E_{RN2}$  were used as input to TRIM. The energy losses of the residual nuclei are shown in figure 6.7.

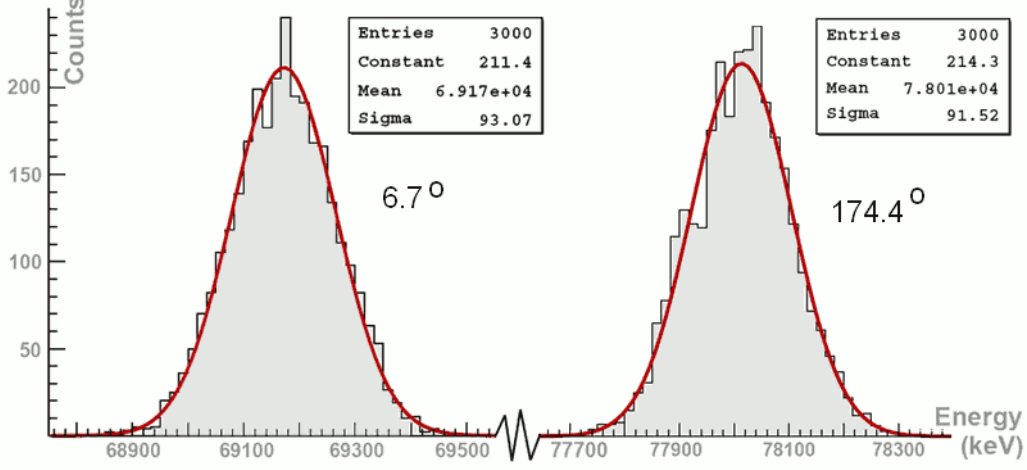


Figure 6.7: TRIM calculations of energy straggling of  $^{52}\text{Cr}$  ions in a  $200 \mu\text{m}/\text{cm}^2$  thick titanium target. In the figure, the kinetic energy distributions of the residual nuclei when they exit the target material are plotted for the case when neutrons are emitted at the angles  $\theta_{n,CM} = 174.4^\circ$  (right) and  $\theta_{n,CM} = 6.7^\circ$  (left) corresponds to initial recoil energy of  $E_{RN1} = 82.4 \text{ MeV}$  and  $E_{RN2} = 73.6 \text{ MeV}$ , respectively.

For the two cases the average energy losses are

$$E_{RN1}^{\text{loss}} = 82.40 \text{ MeV} - 78.01 \text{ MeV} = 4.390 \text{ MeV},$$

which gives the velocity

$$\frac{\Delta v_{RN1}^{\text{loss}}}{c} = \sqrt{\frac{2}{m_{RN1}c^2}} \left( \sqrt{E_{RN1,in}} - \sqrt{E_{RN1,out}} \right) = 1.5760 \cdot 10^{-3}. \quad (6.1)$$

And

$$E_{RN2}^{\text{loss}} = 73.60 \text{ MeV} - 69.17 \text{ MeV} = 4.430 \text{ MeV},$$

which gives the velocity

$$\frac{\Delta v_{RN2}^{\text{loss}}}{c} = \sqrt{\frac{2}{m_{RN2}c^2}} \left( \sqrt{E_{RN2,in}} - \sqrt{E_{RN2,out}} \right) = 1.6858 \cdot 10^{-3}. \quad (6.2)$$

Next, the effects of this energy-loss difference on the Doppler shifts were studied. In the case of the  $^{52}\text{Cr}$  residual nucleus, the  $\gamma$ -ray energy from the  $2^+$  excited state to the  $0^+$  ground state is 1434 keV. For detector position at  $90^\circ$  relative to the incoming beam and a distance of 15 cm from the target to the front face of the detector, which was chosen for these simulations (see section 6.4), the smallest angle for  $\gamma$ -ray detection, which corresponds to the largest Doppler shift, is about  $70^\circ$ . Thus the difference in  $\gamma$  ray energy becomes

$$\Delta E_\gamma = E_{\gamma_0} \cdot \frac{\Delta v_{RN2}^{\text{loss}} - \Delta v_{RN1}^{\text{loss}}}{c} \cos \theta_\gamma = 0.054 \text{ keV}, \quad (6.3)$$

which is a small effect. The contribution from the Doppler shift from this studied effect is hence negligible.

The second target effect concerns the position of the reaction. A new TRIM calculation was performed for  $^{51}\text{V}$  ions with an energy of  $E = 81.6 \text{ MeV}$ . The energy loss of the  $^{51}\text{V}$  beam in the target is shown in figure 6.8.

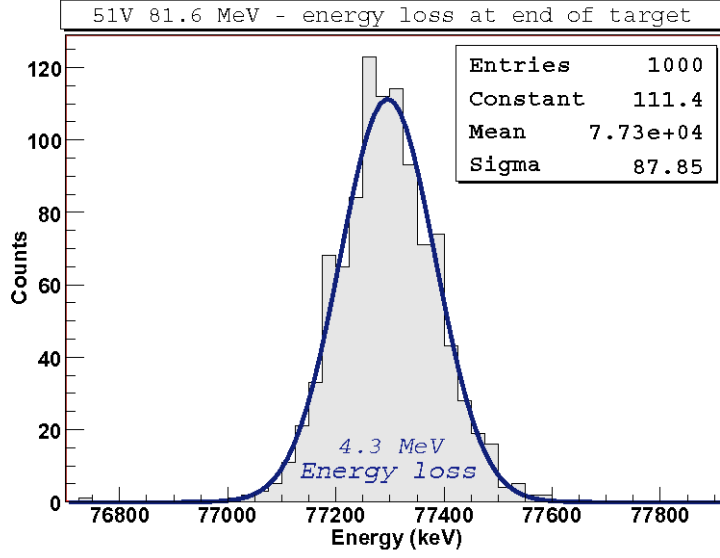


Figure 6.8: Energy distribution of  $^{51}\text{V}$  residual nuclei for the case that the reaction occurs at the end of the target. The energy of the incident  $^{51}\text{V}$  ion beam is 81.6 MeV. The target was a  $200 \mu\text{g}/\text{cm}^2$  thick Ti foil.

The energy loss of the beam through the target is,

$$E_{^{51}\text{V}}^{\text{loss}} = 81.6 - 77.3 = 4.3 \text{ MeV}.$$

From the previous study of  $^{52}\text{Cr}$ , the average of  $E_{\text{RN1}}$  and  $E_{\text{RN2}}$  gives the average energy loss in the case the reactions occur at the beginning of target:

$$E_{^{52}\text{Cr}}^{\text{loss}} = \frac{E_{\text{RN1}} + E_{\text{RN2}}}{2} = 4.41 \text{ MeV}.$$

The velocity of the  $^{52}\text{Cr}$  residual nucleus for the case of a reaction at the end of the target is

$$\frac{v}{c} = 0.0571, \quad (6.4)$$

and

$$\frac{v}{c} = 0.0570, \quad (6.5)$$

if the reaction occurs in the beginning of the target. Note that it is assumed that the  $\gamma$  rays are emitted after the residual nucleus has exited the target (see section ). The difference in velocities is small and gives a negligible effect on the Doppler shifts at  $\theta_\gamma = 70^\circ$ :

$$\Delta E_\gamma = E_{\gamma_0} \cdot \frac{\Delta v}{c} \cos \theta_\gamma = 0.05 \text{ keV}. \quad (6.6)$$

Hence, the position of the reaction in the target can be neglected.

A similar study was done for the  $d(^{37}\text{Cl}, n)$  reaction showing a negligible effect on the Doppler shifts. The average energy loss for the  $d(^{37}\text{Cl}, n)$  reaction was

$$E_{^{37}\text{Cl}}^{\text{loss}} = 3.50 \text{ MeV}. \quad (6.7)$$

## 6.2.2 Angular straggling

In figure 6.9, the angular deviation from the beam direction of the  $^{51}\text{V}$  ions after passing through the  $200 \mu\text{g}/\text{cm}^2$  thick Ti target is shown.

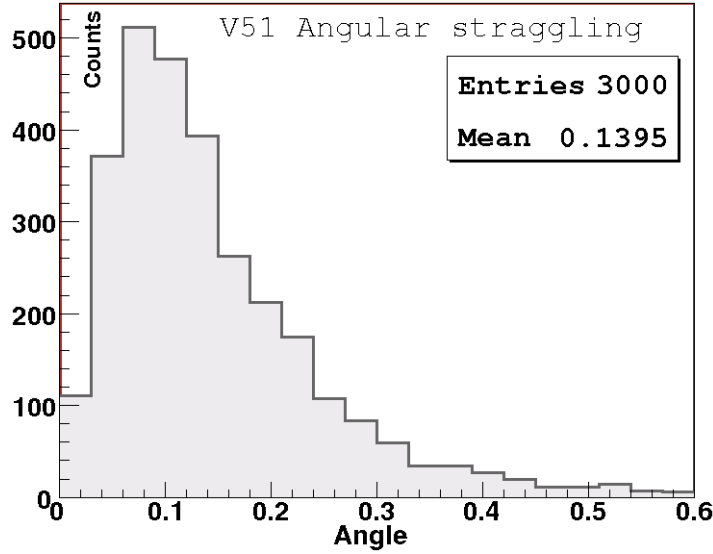


Figure 6.9: Angular straggling of 81.6 MeV  $^{51}\text{V}$  ions in a  $200 \mu\text{g}/\text{cm}^2$  thick Ti target.

The angular distribution of the ions due to straggling has a maximum at  $0.1^\circ$ . This is much smaller than the maximum of the angular distribution due to the neutron emission, see fig. 6.14. Thus, the angular straggling in the target can be neglected.

### 6.2.3 Life-time effects

The compound nucleus has a very short life time compared to the time it takes for it to pass through the target. To prevent the  $\gamma$  rays to be emitted while the residual nucleus is still in the target, it is required that the life time are long enough (see section 4). If the  $\gamma$  rays are emitted while the residual nucleus still is located inside the target a too large spread of Doppler shift will be the result. The average flight distances of the residual nuclei before emitting the  $\gamma$  rays were studied. For the reaction  $d(^{51}\text{V}, n)^{52}\text{Cr}$  the average flight distance  $x$ , before the emission of the  $2^+ \rightarrow 0^+$   $\gamma$ -ray in  $^{52}\text{Cr}$  is

$$x \approx 1.0099\text{ps} \cdot 0.0548c = 1.15 \cdot 10^{-5}\text{m} = 16.5\mu\text{m}, \quad (6.8)$$

which is an order of magnitude larger than the target thickness  $\approx 0.5\mu\text{m}$ . The life-time of the  $2^+ \rightarrow 0^+$  transition in  $^{38}\text{Ar}$  is 0.578 ps and gives

$$x \approx 0.578\text{ps} \cdot 0.0589c = 10.0\mu\text{m}, \quad (6.9)$$

which is also large compared to the target thickness. Thus the photons will be emitted outside the target material in both reactions.

The effective life time of the transitions of interest must also be shorter than the time it takes for the residual nuclei to travel a distance  $\lesssim 1\text{mm}$ . This effect was not studied in the present work.

### 6.2.4 Experimental determination of the intrinsic FWHM

The intrinsic part of the FWHM,  $W_i$ , given in equation 3.10 is unique for every detector type. This value is used as input to the tracking program MGT. Data from a measurement of the core segment of AGATA crystal number C002 using a  $^{226}\text{Ra}$  source [34] was used to obtain the energy dependence of  $W_i$  for a typical AGATA detector. A straight line was fitted to the data points, see fig. 6.10.

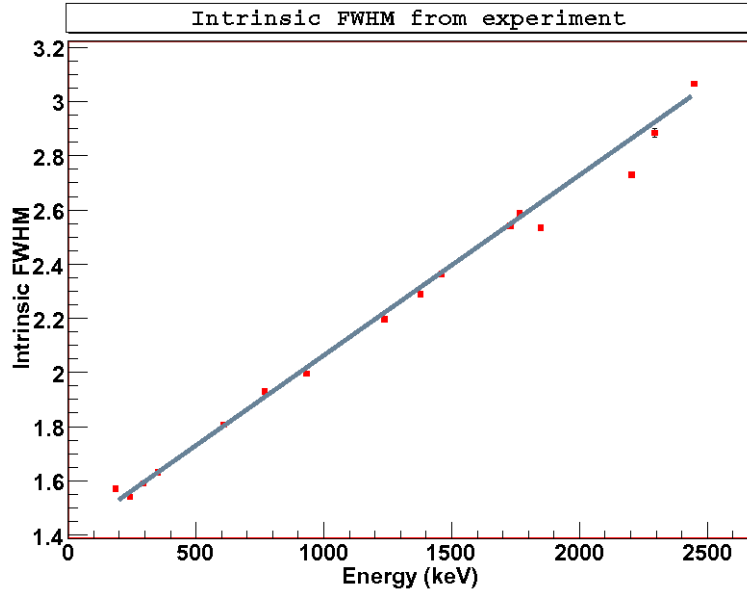


Figure 6.10: Intrinsic FWHM,  $W_i$ , as a function of  $\gamma$ -ray energy for AGATA crystal C002 [34].

Using the fitted straight line of fig. 6.10, the intrinsic FWHM of the peaks corresponding to the 1434keV and 2168keV  $2^+ \rightarrow 0^+$  transitions in  $^{52}\text{Cr}$  and  $^{38}\text{Ar}$  are 2.30keV and 2.83keV, respectively.

## 6.3 evapOR

The studies of the target effect described in section 6.2, yielded an average energy loss in the target of 4.3MeV and 3.5MeV for the  $^{51}\text{V}$  and  $^{37}\text{Cl}$  induced reactions, respectively. The laboratory energies selected for the  $d(^{51}\text{V}, n)^{52}\text{Cr}$  and  $d(^{37}\text{Cl}, n)^{38}\text{Ar}$  reactions were 77.0 MeV and 66.5 MeV, respectively.

### 6.3.1 Energy and angular distributions

Figure 6.11 shows the energy and angular distribution of the neutrons as obtained by evapOR.



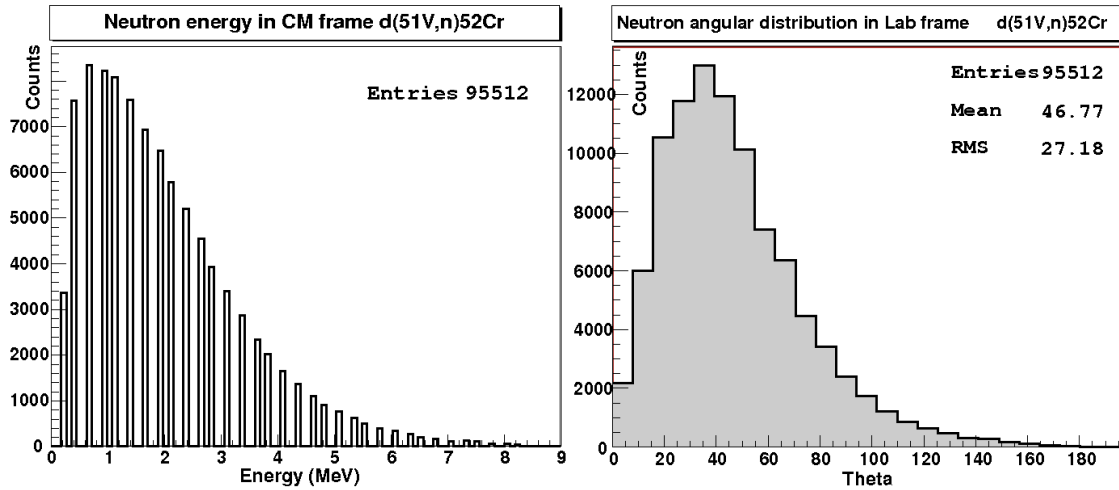


Figure 6.11: The left panel shows the center of mass neutron energy  $E_{CM}^n$  and the right panel shows the angular distribution of the neutrons in the laboratory system,  $\theta_{LAB}^n$  for the reaction  $d(^{51}\text{V}, n)^{52}\text{Cr}$  at  $E(^{51}\text{V}) = 77\text{MeV}$ .

The energy distribution (left hand figure) is Maxwellian as expected from equation 2.11. The distribution has a maximum at about 1MeV. According to the plot on the right hand side of figure 6.11, the neutrons have a large emission angle in the laboratory frame. The centroid of the distribution is around  $40^\circ$ .

Figure 6.12 shows the angular distribution of the neutrons in the center of mass system.

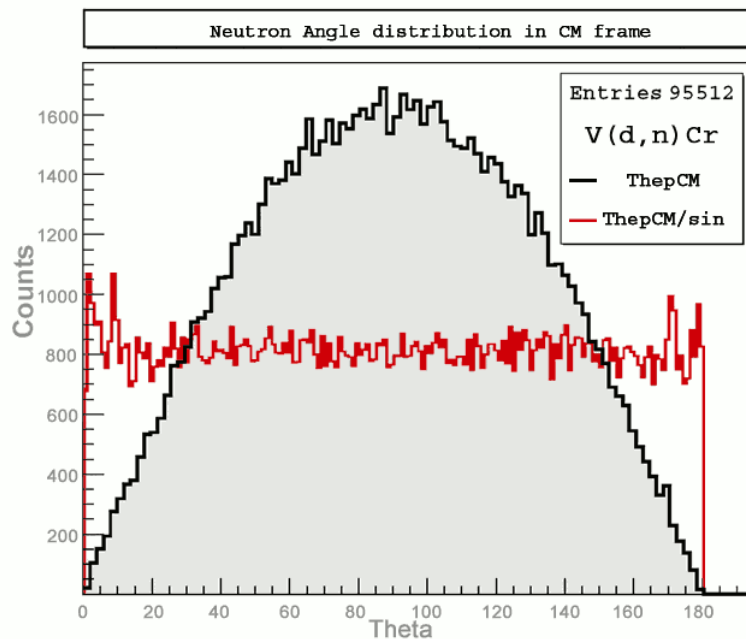


Figure 6.12: Angular distribution of neutrons in the center of mass system for the reaction  $d(^{51}\text{V}, n)^{52}\text{Cr}$  at  $E(^{51}\text{V}) = 77\text{MeV}$ . The black histogram shows the number of neutrons emitted per  $\theta_{CM}$  value. The red histogram is the black histogram divided by  $\sin(\theta_{CM})$ . The histograms are arbitrarily normalized to each other.

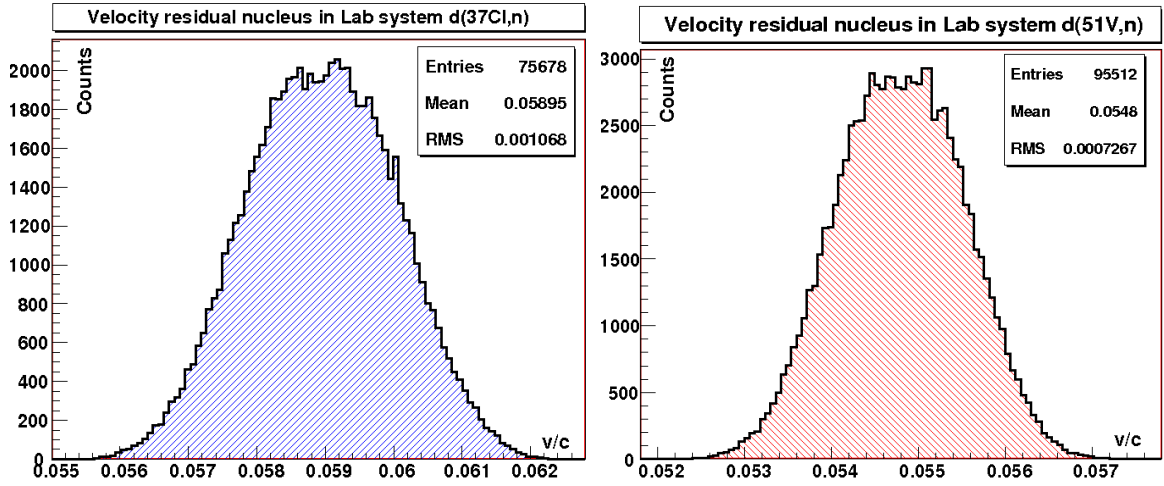


Figure 6.13: Velocity distributions of the residual nuclei for the  $d(^{37}\text{Cl},n)^{38}\text{Ar}$  (left) and  $d(^{51}\text{V},n)^{52}\text{Cr}$  (right) reactions at  $E(^{37}\text{Cl}) = 66.5\text{MeV}$  and  $E(^{51}\text{V}) = 77\text{MeV}$ , respectively.

Figure 6.13 shows the velocity distribution of the residual nuclei in both reactions. The neutron energy distributions in the laboratory frame are shown in the left panel of figure 6.14. The  $d(^{51}\text{V},n)^{52}\text{Cr}$  reaction contains more neutron events and thus the area under the red histogram is larger. The right panel of figure 6.14 shows the angular distributions of the residual nuclei. There is an evident shift of the angular distribution, implying a smaller mean deflection of the  $^{52}\text{Cr}$  nuclei compared to the  $^{38}\text{Ar}$  nuclei. This difference in angular deflection plays a major role in the Doppler shift of the  $\gamma$ -ray energies.

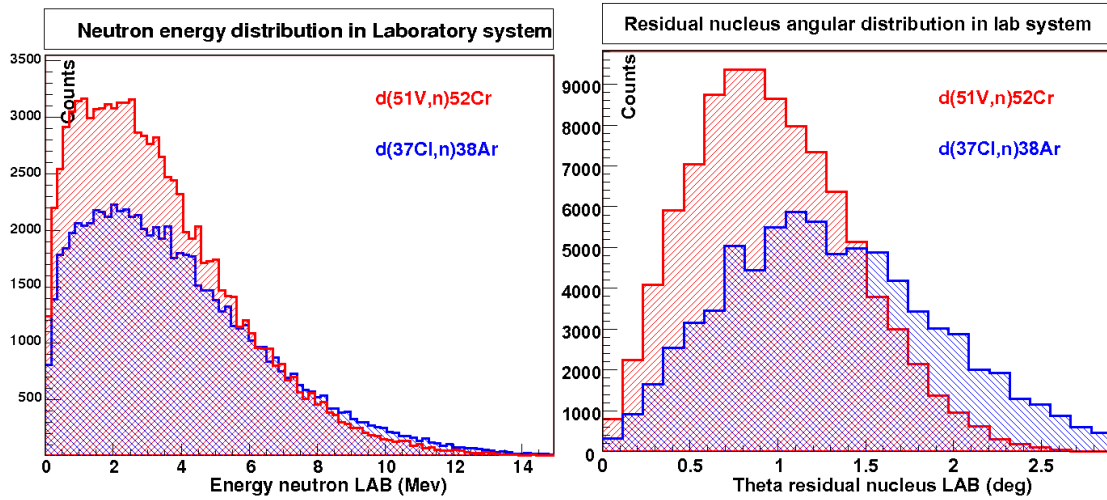


Figure 6.14: The left panel shows the energy distributions of the neutrons and the right panel the angular distribution of the residual nuclei in the laboratory system.

## 6.4 Simulated $\gamma$ -ray spectra

### 6.4.1 Graphical illustration of the GEANT4 simulation

In figure 6.15 a graphical illustration of the GEANT4 simulation is shown. Ten events of the reaction  $^{51}\text{V}(77\text{ MeV}) + d$  were generated by evapOR. The direction of motion of the incoming  $^{51}\text{V}$  beam is from right to left in the figure. For the plot only events belonging to the reaction

channel  $d(^{51}\text{V}, n)^{52}\text{Cr}$  were selected. Each  $^{52}\text{Cr}$  residual nucleus emits one  $\gamma$  ray, with an energy of 1434 keV, corresponding to the  $2^+ \rightarrow 0^+$  transition in  $^{52}\text{Cr}$ .

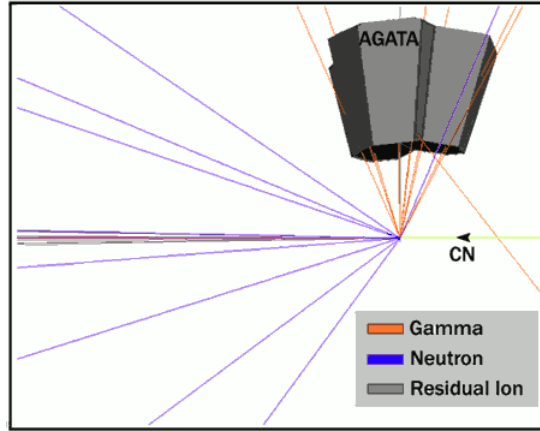


Figure 6.15: A graphical illustration of a GEANT4 simulation in which a compound nucleus emits neutrons and  $\gamma$  rays, which are impinging on an AGATA triple cluster detector. See text for further details.

The  $\gamma$  rays were forced to be emitted isotropically into a cone with an opening angle of  $20^\circ$ , centered at  $90^\circ$  relative to direction of incoming beam. An AGATA triple cluster detector was placed at that angle, and covered a solid angle which was smaller than the solid angle of the  $\gamma$ -ray emission cone. The distance between the  $\gamma$ -ray source and the front of the HPGe crystals was 15 cm in the figure.

Except if otherwise noted, the setup shown in fig. 6.15, with the angle and distance given above, was used in the simulations presented in the following subsections.

#### 6.4.2 Gamma-ray spectrum produced by summing

As a first simple test, a  $\gamma$ -ray spectrum was created by summing for each event the total energy deposited in the detector. Such a spectrum is shown in fig. 6.16 for the 2168 keV  $\gamma$  ray emitted in the  $d(^{37}\text{Cl}, n)^{38}\text{Ar}$  reaction at  $E_{\text{LAB}}(^{37}\text{Cl}) = 66.5$  MeV. The  $\gamma$  rays were emitted isotropically into a  $90^\circ \pm 0.5^\circ$  cone. The intrinsic energy resolution was set to 0 ( $W_i = 0$  keV) and no Doppler corrections were applied. The full-energy peak, the single- and double-escape peaks, and Compton background are clearly visible in the spectrum.

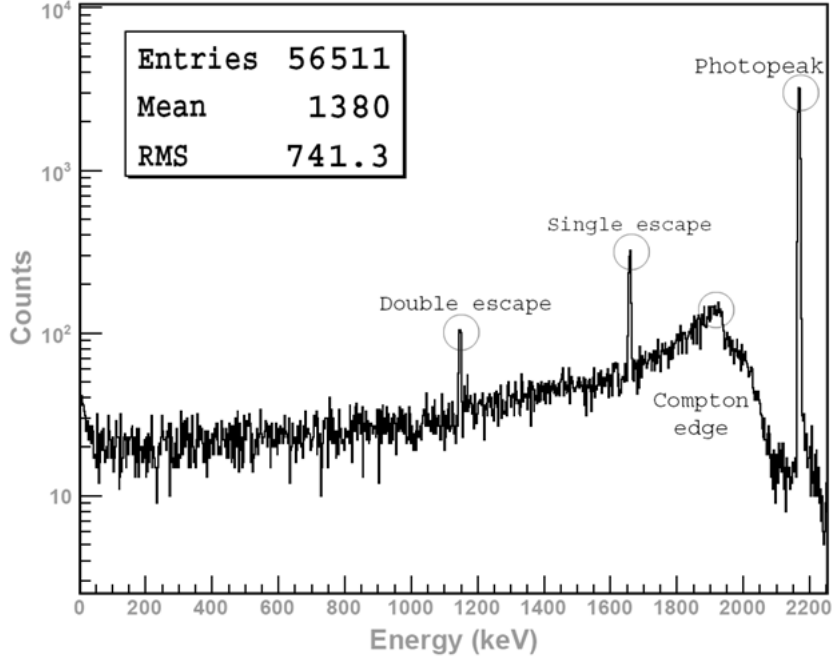


Figure 6.16: A  $\gamma$ -ray spectrum obtained by summing the total energy absorbed in the AGATA triple cluster detector. A total of  $10^5$  evapOR events of the reaction  $^{37}\text{Cl}(66.5\text{ MeV}) + d$  were generated. See text for further details.

### 6.4.3 Gamma-ray spectra produced by tracking and Doppler correction

Tracked  $\gamma$ -ray energy spectra were created by feeding the output of the GEANT4 simulation into the MGT tracking program. The MGT smearing parameter, which emulates a finite interaction position resolution in the HPGe crystals, was used as one of the parameters in the simulations.

The  $\gamma$ -ray emission angle, which is needed by the Doppler correction procedure, was calculated by assuming that the  $\gamma$  rays were emitted from the center of AGATA and detected at the first interaction point, which was obtained from MGT. For the Doppler correction the velocity vector of the residual nucleus is also needed. Except where otherwise noted, an average value of the velocity vector was used, namely an angle of  $0^\circ$  (motion parallel to the beam) and the average velocity given by the evapOR simulation. The use of such average values is common in fusion-evaporation reactions, when no ancillary detector is available for the event-by-event detection of the velocity vector of the residual nuclei.

Initially, two simulations were performed to verify that the tracking and Doppler correction procedures functioned as expected. In the first simulation, shown in the left panel of fig. 6.17, the 1434 keV  $\gamma$  rays from the reaction  $d(^{51}\text{V}, n)^{52}\text{Cr}$ , at  $E_{\text{LAB}}(^{51}\text{V}) = 77.0$  MeV, were emitted at an angle of exactly  $90^\circ$  relative to the incoming beam. Gamma-ray tracking with a 5 mm smearing was used, but no Doppler corrections were applied. In the second simulation, shown in the right panel of fig. 6.17, the 1434 keV  $\gamma$  rays were emitted isotropically into the  $90^\circ \pm 20^\circ$  cone covering the solid angle subtended by the triple cluster detector, and both tracking (with 5 mm smearing) and Doppler corrections were applied. The distance from the source to the front of the HPGe crystals was 15.0 cm. The FWHM of the 1434 keV peak in both panels of fig. 6.17 are almost identical, which shows that the  $\gamma$ -ray tracking and Doppler correction algorithms functioned as expected.

Reaction	$E_\gamma$ [keV]	$W$ [keV]	$W_i$ [keV]	$W_D$ [keV]
$d(^{37}\text{Cl}, n)^{38}\text{Ar}$	2168	7.74	2.83	7.20
$d(^{51}\text{V}, n)^{52}\text{Cr}$	1434	4.55	2.30	3.93

Table 6.2: Contributions to the total FWHM,  $W$ , due to the intrinsic resolution,  $W_i$ , and the Doppler effects,  $W_D$ , for the two studied reactions.

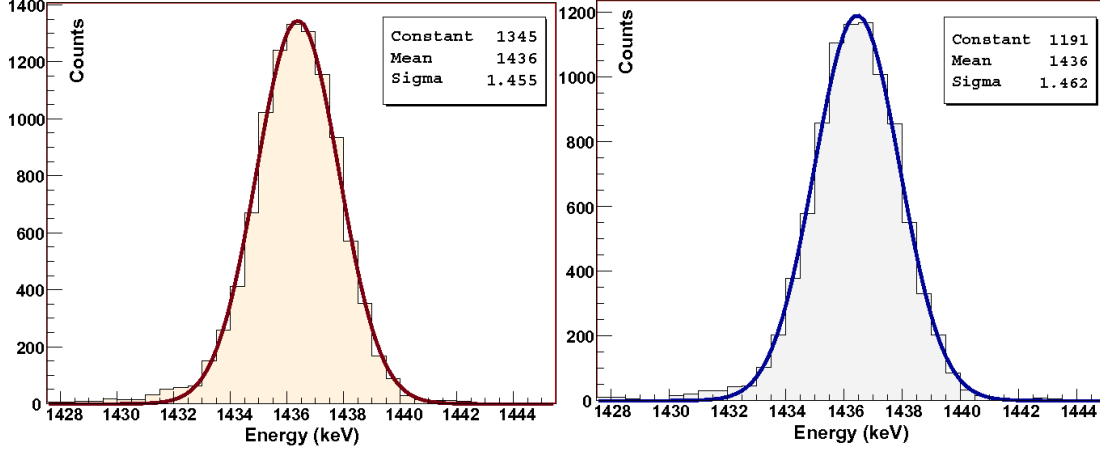


Figure 6.17: Spectra of tracked  $\gamma$  rays emitted in the reaction  $d(^{51}\text{V}, n)^{52}\text{Cr}$  at  $E_{\text{LAB}}(^{51}\text{V}) = 77.0$  MeV. Left: The  $\gamma$  rays were emitted at exactly  $90^\circ$  relative to the incoming beam and no Doppler correction was applied. Right: The  $\gamma$  rays were emitted isotropically into a  $90^\circ \pm 20^\circ$  cone covering the solid angle subtended by the triple cluster detector, and a Doppler correction was applied. See text for further details.

Results of tracked and Doppler corrected  $\gamma$ -ray spectra from simulations in which also the energy dependence of the intrinsic energy resolution (see section 6.2.4) has been included, are shown for the two reaction in fig. 6.18 and 6.19. The smearing parameter was kept at 5 mm and the  $\gamma$  rays were emitted isotropically into the  $90^\circ \pm 20^\circ$  cone.

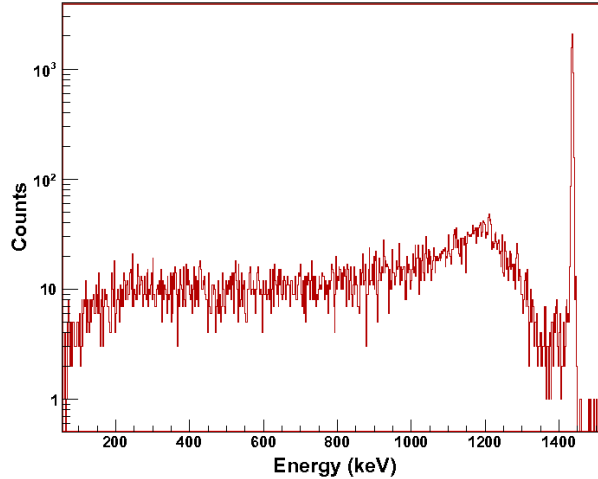


Figure 6.18: Tracked and Doppler corrected  $\gamma$ -ray spectrum of the 1434 keV  $\gamma$  rays emitted in the reaction  $d(^{51}\text{V}, n)^{52}\text{Cr}$ . See text for further details.

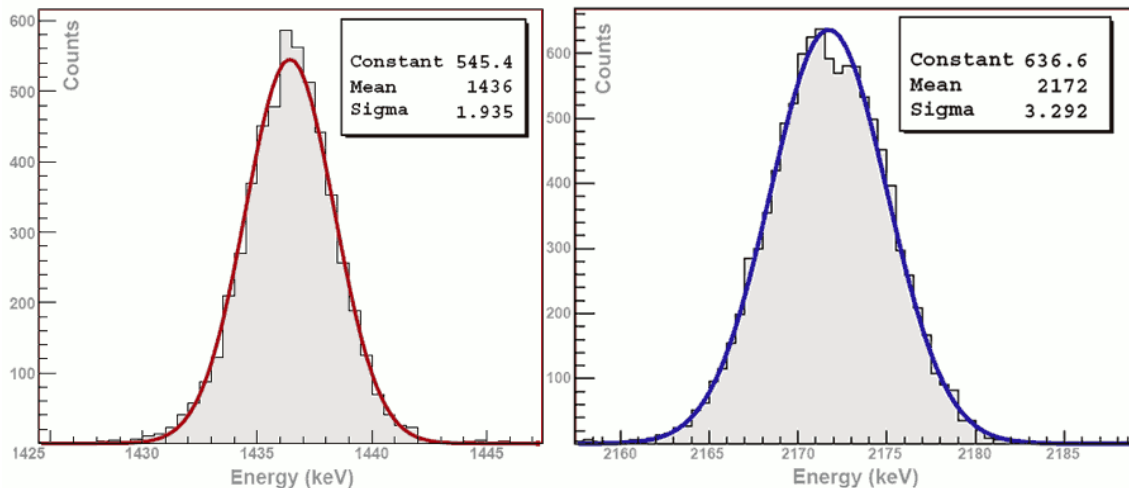


Figure 6.19: Tracked and Doppler corrected  $\gamma$ -ray spectra of the 1434 keV (left) and 2168 keV (right)  $\gamma$  rays emitted in the reactions  $d(^{51}\text{V}, n)^{52}\text{Cr}$  ( $E_{\text{LAB}}(^{51}\text{V}) = 77$  MeV) and  $d(^{37}\text{Cl}, n)^{38}\text{Ar}$  ( $E_{\text{LAB}}(^{37}\text{Cl}) = 66.5$  MeV), respectively. See text for further details.

Numerical values of the total FWHM  $W$  of the peaks in fig. 6.19, and their components (see eq. 3.9) due to the intrinsic resolution ( $W_i$  obtained from fig. 6.10) and due to the Doppler effects  $W_D$ , are given in table 6.1.

The results given in the table clearly show that the contribution to the total FWHM, due to the Doppler effects, is much larger in the reaction  $d(^{37}\text{Cl}, n)^{38}\text{Ar}$  than in the reaction  $d(^{51}\text{V}, n)^{52}\text{Cr}$ . The main reason for this is the difference in mass number of the compound nuclei  $^{38}\text{Ar}$  and  $^{52}\text{Cr}$ . This mass difference leads to a somewhat larger and broader velocity distribution of the residual nuclei (see fig 6.13) and, more importantly, to an angular distribution of the residual nuclei which is both broader and has a maximum at a larger angle (see right panel of fig. 6.14) for the reaction  $d(^{37}\text{Cl}, n)^{38}\text{Ar}$  compared to  $d(^{51}\text{V}, n)^{52}\text{Cr}$ . The angular and velocity distributions of the  $\gamma$ -ray emitting residual nuclei influence directly the Doppler effects, which is seen as an effect on the FWHM of the peaks.

A simulation was also performed by correcting for the Doppler effects introduced by the variation the velocity vector of the residual nucleus. A comparison of the FWHM of the 1434 keV peak obtained when using the average velocity vector and the precise value, as obtained event-by-event from the evapOR simulation, is shown in fig 6.20. For the reaction  $d(^{51}\text{V}, n)$  at  $E_{\text{LAB}}(^{51}\text{V}) = 77.0$  MeV the FWHM is improved from 4.7 keV to 3.9 keV when the precise value of the velocity vector of the residual nucleus is applied in each event.

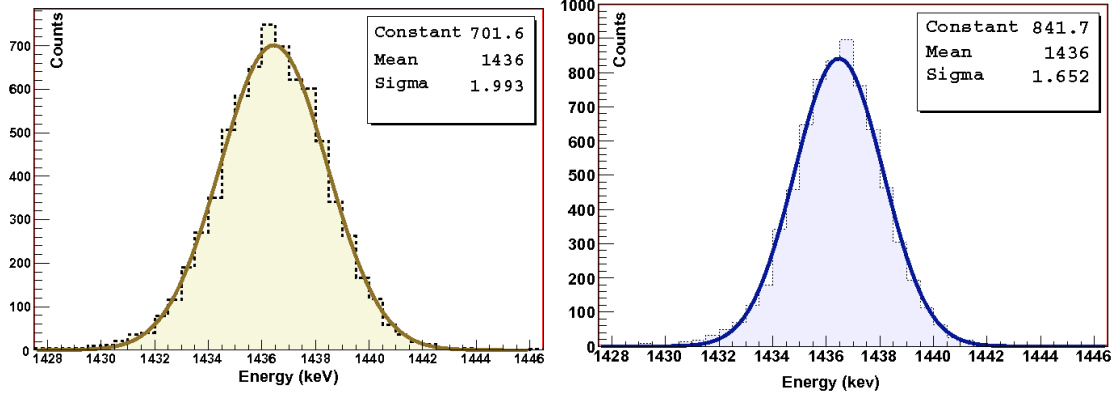


Figure 6.20: Comparison of the FWHM of the 1434 keV peak when the Doppler correction was performed by using for the residual nucleus an average velocity of  $v/c = 0.0548$  and an angle of  $0^\circ$  (left) and the exact value obtained event-by-event from evapOR (right). The reaction was  $d(^{51}\text{V}, n)^{52}\text{Cr}$  at  $E_{\text{LAB}}(^{51}\text{V}) = 77.0$  MeV, the smearing parameter was 5 mm.

#### 6.4.4 Doppler effects induced by emission of $\alpha$ particles

A simulation of Doppler effects, following a reaction channel in which  $\alpha$  particles are emitted, is shown in fig. 6.21. The emitted  $\alpha$  particles are four times heavier than neutrons and have much higher kinetic energies in the laboratory system (compare the left panels of fig. 6.14 and 6.21), which leads to very large spreads both of the energy and angle of the residual nuclei. This in turn leads to very broad  $\gamma$ -ray peaks, as seen in the right panel of fig. 6.21. Thus, for reaction channels with emission of  $\alpha$  particles it is usually necessary to determine event-by-event the velocity vector of the residual nuclei.

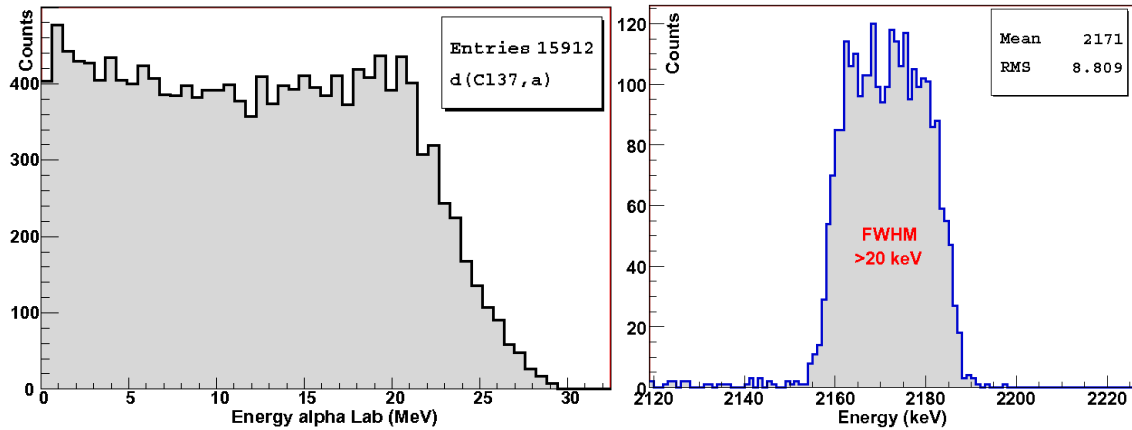


Figure 6.21: Doppler effects following the reaction  $d(^{37}\text{Cl}, \alpha)^{35}\text{S}$  at  $E_{\text{LAB}}(^{37}\text{Cl}) = 66.5$  MeV. Left: Kinetic energy distribution of the residual nuclei  $^{35}\text{S}$ . Right: FWHM of a  $\gamma$ -ray peak at 2168 keV after tracking using the average residual nucleus velocity vector for the Doppler correction. The smearing parameter was 5 mm.

#### 6.4.5 FWHM as a function of smearing parameter

Simulations, in which the total FWHM of the 1434 keV and 2168 keV peaks were determined as a function of the MGT smearing parameter, are shown in figures 6.22 and 6.23 for two different detector distances, 15.0 cm and 23.5 cm, respectively. As seen in the figures, the slopes increase for small values of the smearing parameter, up to about 4-8 mm and become more or less constant for larger values. The slopes are quite similar in all cases, although slightly larger for the  $d(^{51}\text{V}, n)^{52}\text{Cr}$  reaction and for the shorter distance of 15.0 cm.

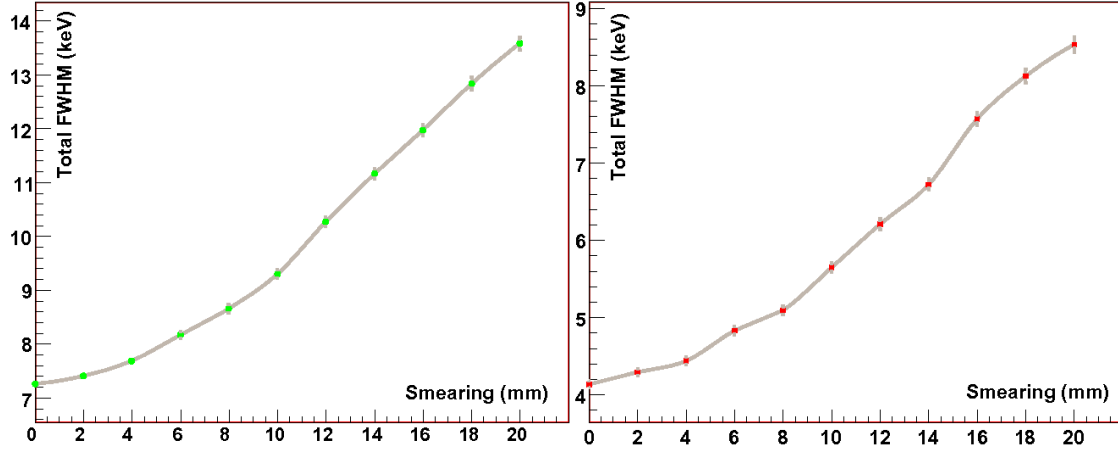


Figure 6.22: FWHM as a function of the MGT smearing parameter for the 2168 keV (left) and 1434 keV (right) peaks of the  $d(^{37}\text{Cl}, n)^{38}\text{Ar}$  and  $d(^{51}\text{V}, n)^{52}\text{Cr}$  reactions, respectively. The distance from the source to the front of the HPGe crystals was 15.0 cm. The data points are connected by straight lines.

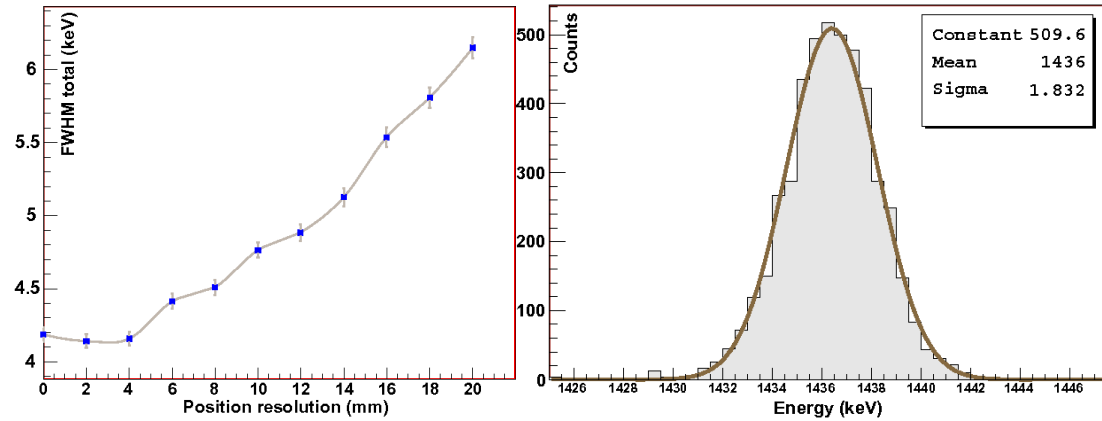


Figure 6.23: Same as fig. 6.22 but for a distance of 23.5 cm from the source to the front of the HPGe crystals.

The interaction position resolution which is expected for the AGATA HPGe crystals is of the order of 5 mm, a value which, however, is not constant. The resolution will depend on the position of the interaction in the crystal. For example in the front part of the crystal, where the electric field is rather non-uniform, the interaction position resolution will be worse compared to a position in the central parts. The interaction position resolution will also depend on the energy deposited in the interaction point. It is expected that it will be proportional to the inverse square root of the interaction energy, a dependence which is implemented in MGT, although not used in this work.

A conclusion of the results shown in fig. 6.22 and 6.23 is that with the proposed reactions,  $d(^{37}\text{Cl}, n)^{38}\text{Ar}$  at  $E_{\text{LAB}}(^{37}\text{Cl}) = 66.5$  MeV and  $d(^{51}\text{V}, n)^{52}\text{Cr}$  at  $E_{\text{LAB}}(^{51}\text{V}) = 77.0$  MeV, it will be difficult to get a good determination of the interaction position resolution from the measured FWHM of the peaks. One possibility to improve the sensitive, is to make the measurements for much smaller distances, than what was used in this work (15.0 cm and 23.5 cm). Another possibility is to try to find another reaction with larger average recoil velocities but which still has small enough spread of the residual nucleus velocity vector so that the average Doppler correction procedure may be used.



## 6.5 Conclusions and summary

In section 6.1 the studied reactions in TALYS resulted in two interesting reactions for further study, namely  $d(^{51}\text{V}, n)^{52}\text{Cr}$  and  $d(^{37}\text{Cl}, n)^{38}\text{Ar}$ . On the basis of the requirements in section 4, these reactions have suitable  $\gamma$ -ray energies and life times within the required range. Both reactions have dominant cross sections for the desired neutron channel. Both reactions lead to even-even residual nuclei and give quite large recoil velocities (important in order to study the Doppler effects).

In section 6.2, the target effects were investigated using TRIM. Two major sources of unwanted target effects were studied and determined to be negligible for the Doppler shifts. The average energy loss for the ions in the target material were simulated and presented.

In section 6.3, results from *evapOR* and TALYS were compared. Different energy and angular distributions were produced by *evapOR*. Due to the different amount of nucleons in the compound nuclei of the two reactions, the  $^{38}\text{Ar}$  residual nuclei were deflected more from the ion beam direction compared to  $^{52}\text{Cr}$ . This difference in angular deflection is the reason why the Doppler broadening is larger for the reaction  $d(^{37}\text{Cl}, n)^{38}\text{Ar}$  than for  $d(^{51}\text{V}, n)^{52}\text{Cr}$ .

In section 6.4 the detection of the  $\gamma$  rays in one AGATA triple cluster detectors was simulated with GEANT4. The  $\gamma$  rays were tracked by the MGT tracking program to produce Doppler corrected  $\gamma$ -ray spectra. The FWHM of the  $\gamma$  ray peaks of interest were calculated as a function of the interaction position resolution. The  $d(^{51}\text{V}, n)^{52}\text{Cr}$  reaction was found to be slightly more suitable than the  $d(^{37}\text{Cl}, n)^{38}\text{Ar}$  reaction for the planned AGATA commissioning experiment.

# Appendix A

## Acknowledgment

This diploma work could not have been fulfilled without the great support, aid and guidance from two excellent supervisors. Professor Johan Nyberg and the PhD student, Pär-Anders Söderström. Johan shared his knowledge generously and delivered me a comprehensive introduction into the field of nuclear physics research. His supervising showed wide patience and broad capacity of describing the tasks and the methods of solving them. Pär-Anders, I am obliged to you, for all hours with programming support. All our general and specific discussion about physics, truly enlightened my mind. It was important for me to share that room with you in order to collect as much as possible of your experience. I would like to thank all the people at the division of nuclear and particle physics, it was a pleasure to write the diploma work among you people. Thanks for my opponent Pelle who gave me a proper review of my report. Special thanks for Mikael, Emma, Bengt, Patrik, Carl-Oscar, Samson, Vasily, Pernilla, Riccardo, Henrik and Henrik. I want also to pay my respect for professor Jan Blomgren who supported and guided during my application for the PhD position.

My deepest gratitude goes to my dear family. You are always present, no matter the circumstances. This diploma work is dedicated to my fantastic parents, who I stand in obligation to for my upbringing. You supported me in my choices through life, that meant everything for me. My siblings, Amir and Afnan, you are making me proud. My dear Sheima, thanks for painting my entire world.

My friends, you have your part in this as well. Greetings to Alaa, Alvaro, Martin, PO, Rickard, Jonatan, Fabrice, Chi, Ludde, Mortada, Ali, Niklas, Jan, Tassilo, Miguel, Hans-Erik, Pedro, Zeyd and all you others.

## Appendix B

# Available ion beams at Laboratori Nazionali di Legnaro (Padova)

Table B.1: Available ion beams at LNL

Beam	Current in (nA)	Beam	Current in (nA)	Beam	Current in (nA)
1H	1000	40Ca	150	79Br	800
2H	300	48Ca	150	81Br	800
6Li	50	48Ti	700	90Zr	100
7Li	200	50Cr	150	91Zr	25
10B	100	52Cr	150	92Zr	30
11B	400	51V	250	94Zr	30
12C	3000	54Fe	200	96Zr	300
13C	35	56Fe	200	92Mo	250
14N	800	58Ni	1500	94Mo	150
16O	2000	60Ni	500	95Mo	250
17O	500	64Ni	500	96Mo	250
18O	500	63Cu	1000	97Mo	150
19F	3000	65Cu	350	98Mo	400
24Mg	300	64Zn	500	100Mo	150
26Mg	200	66Zn	250	96Ru	200
27Al	400	68Zn	200	98Ru	70
28Si	1000	69Ga	300	99Ru	450
29Si	300	70Zn	200	100Ru	450
30Si	200	71Ga	200	101Ru	600
31P	500	74Ge	800	102Ru	1000
32S	2000	76Ge	200	104Ru	650
33S	400	76Se	200	107Ag	400
34S	200	77Se	300	109Ag	400
36S	400	78Se	1000	127I	800
35Cl	2000	80Se	2000	197Au	500
37Cl	650	82Se	400		

# Appendix C

## Simulation steps

### 1. evapOR

- Run evapOR.
- Modify the \*.inp file for evapOR, where you can choose nuclei, spin and energy.
- evapOR-loop
- evapOR-loop \*.inp

You will have now some produced files. The important one is \*.pax

### 2. Sortpax:

You run sortpax to generate the Doppler shifted gammas and to produce the \*.aga file.

- sortpax \*.pax
- choose aga file with typing '\*.aga'
- choose txt file to read the events, with typing '\*.txt'
- choose bin file for evapOR Root tree, with typing '\*.bin'
- choose the gate on nucleus (Z, N)
- choose the angle of emitted photons (thetamin, thetamax, phimin, phimax)

Now you will have the \*.aga file. (This you copy to fari in my case)

### 3. AGATA Geant4:

Go to directory of AGATA GEANT4

- Run 'Agata -Ext -n' in order to read the particles also.
- Type the desired of the following commands
  - /Agata/file/enableLM
  - /Agata/file/verbose 1 to write information
  - /Agata/file/packingDistance 5. for packing
- Define the geometry, a cluster is given by this macro
  - /control/execute macros/geom180Ali.mac

- Look in macro file and manual agata GEANT4 to see the other geometries. The distance to the detector is given in A180eulerAli.list which is under the folder A180. You can there put and move the detector anywhere.

To generate with the \*.aga file use

- /Agata/generator/emitter/eventFile /home/tsl0/ali/Desktop/doppler.aga /Agata/run/beamOn 100000

To generate with AGATA

- /Agata/generator/recoil/beta 5. (for nuclei's velocity)
- /Agata/generator/gamma/energy 1000 (the energy of gammas)
- /Agata/generator/gamma/thetaRange 65.0 115.0 (the  $\theta$  angle emitted gammas)
- /Agata/generator/gamma/phiRange 65.0 115.0 (the  $\phi$  angle emitted gammas)

#### 4. MGT:

The output is gammaevents.0000/1/2..... and this should be used in MGT go the folder where this file is and type

- ' mgt -fw 0 0 -f GammaEvents.0000 -ll 0 -oa 30 30 -dd 5 5 -sr 0.05 0 0 '

where fw is defining the intrinsic FWHM, statistical and then noise factor. ll 0/1/2/3 gives more information. dd defines the smearing and packing .

- sr gives the average velocity and direction in  $\theta$  and  $\phi$ .

# Bibliography

- [1] I. Y. Lee, M. A. Deleplanque, and K. Vetter. Developments in large gamma-ray detector arrays. *Reports of Progress in Physics*, **66**:1095, 2003.
- [2] J. Simpson. The AGATA Project. *Journal of physics:Conference Series*, **41**:72, 2006.
- [3] G. A. Jones. *The Properties of Nuclei*. Oxford Science Publications, Oxford, 2nd edition, 1987.
- [4] B. Höistad. Lecture notes nuclear physics nv2, 2008.
- [5] G. R. Satchler. *Introduction to Nuclear Reactions*. The Macmillan press LTD, 1980.
- [6] R. Bock. *Heavy Ion Collisions*, volume 2. North-Holland, 1980.
- [7] D. G. Swanson and N. T. Porile. Statistical-Model Calculation of the Angular Distributions of (a, n) Reaction Products. *Phys. Rev.*, **C1**:4, 1970.
- [8] D. W. Lang and K. J. Le Couteur. Pairing energy effects in excited nuclei. *Nuclear Physics*, **14**:21, 1959.
- [9] T. Ericson and V. Strutinsky. On Angular Distributions in Compound Nucleus Processes. *Nuclear Physics*, **9**:689, 1958.
- [10] A. Einstein. On a Heuristic Viewpoint Concerning the Production and Transformation of Light. *Annalen der Physik*, **17**:132, 1905.
- [11] A. H. Compton. A Quantum Theory of the Scattering of X-rays by Light Elements. *Phys. Rev.*, **21**:483, 1923.
- [12] K. S. Krane. *Introductory Nuclear physics*. Wiley, 3rd edition, 1988.
- [13] H. Bethe. Zur Theorie des Durchgangs schneller Korpuskularstrahlen durch Materie. *Annalen der Physik*, **397**:305, 1930.
- [14] R.P.Feynman. *The Feynman lectures on physics*, volume 2. ADDISON-WESLEY, 1963.
- [15] G. F. Knoll. *Radiation Detection and Measurement*. Wiley, 3rd edition, 1999.
- [16] A. Lopez-Martens, et al. Gamma-ray tracking algorithms: a comparison. *Nucl. Inst. Meth.*, **A533**:454, 2004.
- [17] E. Farnea. Private communication, 2008.
- [18] A. J. Koning, S. Hilaire, and M. C. Duijvestijn. TALYS-1.0. In O. Bersillon, et al. (editors), *Proceedings of the International Conference on Nuclear Data for Science and Technology 2007*, page 211. EDP Sciences, 2008.
- [19] J. Ziegler and J. Biersack. *The Stopping and Range of Ions in Solids*. Pergamon Press, New York, 1985.
- [20] J. Beene. Unpublished program evapor, 2008.

- [21] M. Palacz. Private communication, 2008.
- [22] E. Farnea and D. Bazzacco. A Monte Carlo Code for the AGATA Array. In D. R. Napoli, et al. (editors), *LNL Annual Report 2003*, page 158. 2004.
- [23] S. Agostinelli, et al. GEANT4—a simulation toolkit. *Nuclear Instruments and Methods in Physics Research A*, **506**:250, 2003.
- [24] D. Bazzacco. Unpublished program mgt, 2008.
- [25] S.Qiang. SubCoulomb Proton Induced Reactions on Copper. Ph.D. thesis, University of Kentucky, 1990.
- [26] M. Sevier, et al. Absolute Cross Sections of Proton Induced Reactions on Cu-65,Ni-64,Cu-63. *Australian Journal of Physics*, **36**:463, 1983.
- [27] D. M. Drake, et al. The Radiative Capture of Fast Protons by Medium-Mass Nuclei. *Nuclear Physics*, **A203**:257, 1973.
- [28] Z. E. Switkowski, et al. Threshold Effects in Proton-induced Reactions on Copper. *Australian Journal of Physics*, **31**:253, 1978.
- [29] T. Zhenlan, et al. Excitation Function of Deuteron Induced Reactions on Natural Iron. *Atomic Energy Science and Technology*, **5**:506, 1983.
- [30] M. R. Zaman and S. M. Qaim. Excitation functions of (d,n) and (d,a) reactions on high enriched  $^{54}\text{Fe}$ : Relevance to the Production of high purity  $^{55}\text{Co}$  at a small cyclotron. *Radiochimica Acta*, **75**:59, 1996.
- [31] S. Kailas, et al. V-51(p,n)Cr-51 Reaction from Energy of Protons 1.9 to 4.5 MeV. *Pramana*, **24**:629, 1985.
- [32] J. Zyskind, et al. Competition effects in proton-induced reactions on  $^{51}\text{V}$ . *Nuclear Physics*, **A343**:295, 1980.
- [33] A. Gadea. Private communication, 2008.
- [34] A. Wiens. Private communication, 2008.